

***p*-orbital density wave with *d* symmetry in high- T_c cuprate superconductors predicted by the renormalization-group + constrained RPA theory**

Masahisa Tsuchizawa, Youichi Yamakawa, and Hiroshi Kontani

Department of Physics, Nagoya University, Nagoya 464-8602, Japan

(Dated: April 25, 2016)

The discovery of the charge-density-wave formation in the high- T_c cuprate superconductors has activated intensive theoretical studies for the pseudogap states. However, the microscopic origin of the charge-density-wave state has been unknown so far since the many-body effects beyond the mean-field-level approximations, called the vertex corrections, are essential. Toward solving this problem, we employ the recently developed functional renormalization-group method, by which we can calculate the higher-order vertex corrections in a systematic and unbiased way with high numerical accuracy. We discover the critical development of the *p*-orbital-density-wave (*p*-ODW) instability in the strong-spin-fluctuation region. The obtained *p*-ODW state possesses the key characteristics of the charge ordering pattern in Bi- and Y-based superconductors, such as the wave vector parallel to the nearest Cu-Cu direction, and the *d*-symmetry form factor with the antiphase correlation between p_x and p_y orbitals in the same unit cell. In addition, from the observation of the beautiful scaling relation between the spin susceptibility and the *p*-ODW susceptibility, we conclude that the main driving force of the density wave is the Aslamazov-Larkin vertex correction that becomes very singular near the magnetic quantum-critical point.

PACS numbers: 74.72.Kf, 74.20.-z, 74.40.Kb, 75.25.Dk

I. INTRODUCTION

Understanding of the exotic electronic states in underdoped cuprate high- T_c superconductors has been one of the greatest challenges in condensed-matter physics. Especially, the charge-density-wave state observed in various compounds is recognized as a key feature of underdoped cuprate superconductors [1–21]. The x-ray measurements have succeeded in the direct observation of the charge-density waves below ~ 200 K [8, 9]. By means of the resonant x-ray scattering and STM measurements, it has now been recognized in many compounds that (i) the ordering vector of the charge-density wave is of axial type with the wave vector $\mathbf{Q}_a = (\delta_a, 0)$ [8, 9, 11–15, 17–21], and (ii) the charge modulation emerges mainly on the oxygen *p* orbital [12, 17, 20, 21]. In addition, (iii) the symmetry of the charge-order pattern is *d*-wave type, in which the modulations are antiphase between p_x and p_y orbitals in the intra unit cell [12, 17, 20, 21]. The charge-modulation pattern [12, 17, 20, 21] is depicted in Fig. 1(a), which can be regarded as the *d*-symmetry *p*-orbital charge-density-wave (*p*-ODW) state. The density-wave wave vector \mathbf{Q}_a corresponds to wave vector connecting the neighboring “hot spots” shown in Fig. 1(b). The microscopic derivation of the charge-density-wave state with the key properties (i)–(iii) based on the realistic Hubbard model has been desired for years.

Theoretical studies for the pseudogap phenomena have been performed by considering various strong-correlation effects [22–26]. Motivated by the discovery of the density wave below ~ 200 K [8–21], many scenarios of the spin-fluctuation-driven nematic order have been proposed in Refs. [27–44], based on various single-orbital models. Especially, the bond-density-wave (BDW) state [28–37], the pair-density-wave (PDW) state [38–42], and the composite charge orders [43, 44] have been studied. The BDW state is defined as the density wave with *d*-symmetry form factor. As the driving force of the BDW state, the authors in Refs. [28–30, 33, 36]

had focused on the Maki-Thompson vertex correction (VC), in analogy to the *d*-wave superconductivity driven by the Maki-Thompson VC in the Eliashberg theory. The Maki-Thompson process for the BDW instability is shown in Fig. 1(c), which is the first-order term with respect to the spin susceptibility. In general, the Maki-Thompson VC gives the density-wave instabilities at wave vectors $\mathbf{q} = \mathbf{Q}_a$ or \mathbf{Q}_d : The wave vectors \mathbf{Q}_a and \mathbf{Q}_d connect the hot spots on the Fermi surface (FS) shown in Fig. 1(b). The enhancement of the BDW susceptibility was supported by the renormalization-group (RG) method in the weak-coupling region [31, 37]. However, the predominant wave vector is of the diagonal type, \mathbf{Q}_d , inconsistently with experimentally-observed axial nematic order. It was also pointed out that the BDW instability driven by the Maki-Thompson process does not dominate over the superconducting instability [43, 45]. Also, the PDW state has been considered as the origin of the pseudogap phase [39, 40]. The PDW is formed by the linear combination of the Cooper pairs with finite momenta. The PDW is also induced by the Maki-Thompson process [41, 42], although the induced charge modulation has momentum $2\mathbf{Q}_a$ [40]. To realize the density wave with \mathbf{Q}_a , several types of the composite charge order parameters have been proposed [41–44]. However, the *d* symmetry of its form factor has not been explained.

Quite recently, the Aslamazov-Larkin VC was suggested to be more important near the magnetic quantum-critical point [46]. The Aslamazov-Larkin VC is the second-order term with respect to the spin susceptibility [Fig. 1(d)]. The predominant wave vector driven by this VC is of the axial type, \mathbf{Q}_a , due to the important scattering process shown in Fig. 1(b). However, only the single Aslamazov-Larkin process had been studied in Ref. [46]. In addition, the obtained form factor is given by a complex mixture between the *d*- and *p*-orbital charge densities.

In order to settle down the controversy on the driving force of the density wave, we have to employ a sophisticated the-

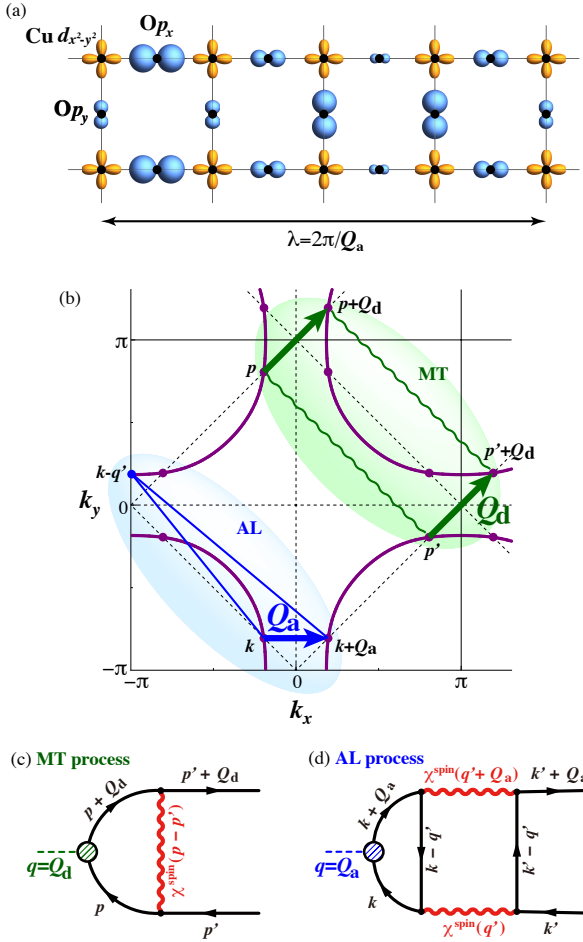


FIG. 1. (a) Schematic charge distribution in the d -symmetry p -ODW state with the wave vector $\mathbf{Q}_a = (0.5\pi, 0)$. The size of the orbitals represents the charge density. (b) The Fermi surface of the cuprate superconductors. The density-wave instabilities due to the VCs emerge at $\mathbf{Q}_d = (\delta_d, \delta_d)$ and $\mathbf{Q}_a = (\delta_a, 0)$, both of which connect the hot spots. (c) The Maki-Thompson (MT) process [30, 33, 36] and (d) the Aslamazov-Larkin (AL) process [46], which are the first-order and second-order terms with respect to the spin susceptibility, respectively. The scattering process in the Maki-Thompson VC, expressed by $G(\mathbf{p}) G(\mathbf{p} + \mathbf{Q}_d) G(\mathbf{p}') G(\mathbf{p}' + \mathbf{Q}_d)$, is shown by green lines in (b). Also, the important scattering process in the Aslamazov-Larkin VC, which is expressed by $G(\mathbf{k}) G(\mathbf{k} + \mathbf{Q}_a) G(\mathbf{k} - \mathbf{q}')$ in the three-point vertex, is shown by blue lines where $\mathbf{q}' \approx \mathbf{Q}_s$ (the wave vector of the spin fluctuation).

oretical method to calculate higher-order diagrams, including both Maki-Thompson and Aslamazov-Larkin VCs, in a systematic and unbiased way. For this purpose, the functional RG method would be the most appropriate theoretical technique. This method enables us to calculate various types of VCs up to the parquet-approximation level, in which the infinite series of the Maki-Thompson and Aslamazov-Larkin VCs are included. The RG method has been successfully applied in the one-dimensional electron systems [47, 48] and has been developed as a powerful method for two-dimensional strongly-correlated electron systems [49–57].

In this paper, we employ the recently developed improved functional RG method, called the RG+constrained RPA (cRPA) method [58, 59], in order to tackle the unsolved theoretical problem on the charge-density-wave state. By utilizing this method, we can evaluate the momentum dependence of susceptibilities with high accuracy. We examine various charge and spin susceptibilities in the realistic three-orbital d - p Hubbard model [60, 61]. We discover that the susceptibility of the d -symmetry p -ODW state is critically enhanced at the wave vector \mathbf{Q}_a in the strong-spin-fluctuation region. The obtained p -ODW state explains satisfactorily the experimental key features (i)–(iii) listed above. Thus, we predict that the p -ODW with d symmetry [Fig. 1(a)] is the origin of the density wave in cuprate superconductors. The beautiful scaling between the spin and p -ODW susceptibilities means that the main driving force of the charge-density instability at \mathbf{Q}_a is the Aslamazov-Larkin VC, which is more singular than the Maki-Thompson VC near the magnetic quantum-critical point. Therefore, the p -ODW in cuprates originates from the strong interference between the spin and orbital fluctuations, which is described microscopically as the vertex corrections.

This paper is organized as follows. In Sec. II, we introduce the three-orbital d - p model and explain the key idea of the RG+cRPA theory. In Sec. III, we show the numerical results on the spin, p -ODW, and d -orbital BDW susceptibilities. In the weak-spin-fluctuation region, the diagonal density susceptibilities are moderately enhanced by the Maki-Thompson VC, consistently with the previous results [31, 33, 36, 37]. In the strong-spin-fluctuation region, in contrast, the axial p -ODW susceptibility is critically enhanced by the Aslamazov-Larkin VC, dominating over the BDW susceptibility. In Sec. IV, we show the beautiful scaling relation between the spin and charge susceptibilities, which means that the instability at $\mathbf{q} = \mathbf{Q}_a$ is driven by the Aslamazov-Larkin VC. We briefly discuss the effect of the Coulomb interaction for p orbital. Section V is devoted to conclusions. Details of the technical calculations are given in Appendixes, where the comparison between the conventional patch-RG and the RG+cRPA theories are also made for the present three-orbital d - p model.

II. d - p HUBBARD MODEL AND RG+CRPA METHOD

We investigate a standard three-orbital d - p Hubbard model [60, 61], shown in Fig. 1(a), which has been analyzed for understanding the charge-density-wave state on the oxygen p orbital [46, 62, 63]. Its Hamiltonian is given by

$$H_{dp} = \sum_{\mathbf{k}, \sigma} c_{\mathbf{k}, \sigma}^\dagger \hat{H}_0(\mathbf{k}) c_{\mathbf{k}, \sigma} + U_d \sum_j n_{d,j,\uparrow} n_{d,j,\downarrow}, \quad (1)$$

where $c_{\mathbf{k}, \sigma}^\dagger = (d_{\mathbf{k}, \sigma}^\dagger, p_{x, \mathbf{k}, \sigma}^\dagger, p_{y, \mathbf{k}, \sigma}^\dagger)$ is the creation operator for the electron on $d_{x^2-y^2}$, p_x , and p_y orbitals with wave vector \mathbf{k} and spin σ . The d -electron density operator is $n_{d,j,\sigma} = d_{j,\sigma}^\dagger d_{j,\sigma}$. We only consider the on-site Coulomb interaction for the d orbital U_d and the effect of intersite Coulomb interaction is briefly discussed later. For the kinetic term $\hat{H}_0(\mathbf{k})$, we use the first-principles hopping integrals for La_2CuO_4 in Ref. [64] (See the note in Ref. [65]). In addition, we introduce the third-nearest d - d hopping -0.1 eV to make the FS closer

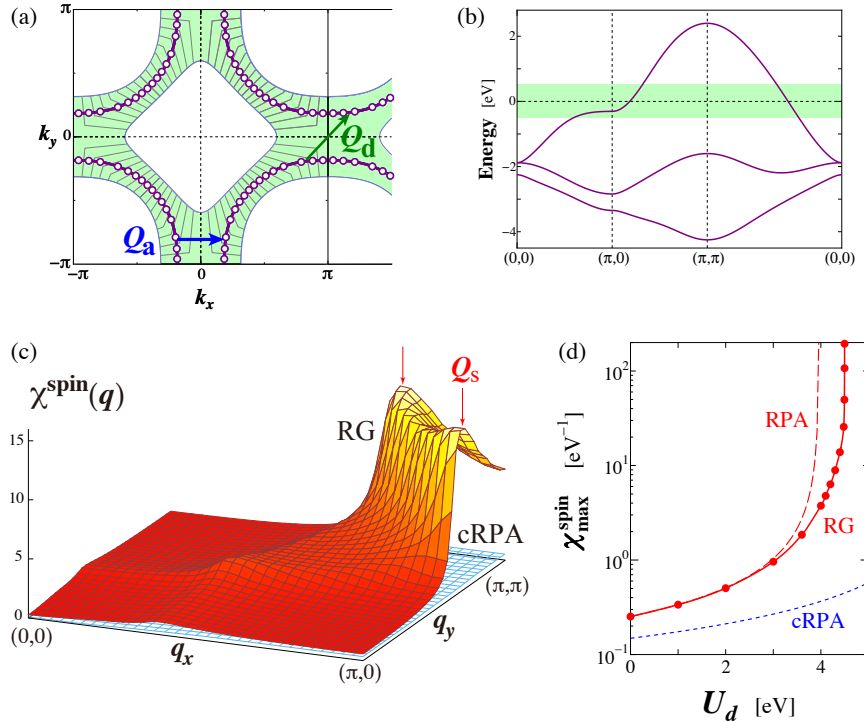


FIG. 2. (a) The Fermi surface and (b) the band structure in the present three-orbital d - p model. The low-energy region ($|E| < 0.5$ eV) are denoted by the shaded areas. The N_p -patch discretization for $N_p = 64$ is shown in (a), whereas we set $N_p = 128$ in the numerical study of the present paper. (c) The obtained spin susceptibility for the d orbital $\chi^{\text{spin}}(\mathbf{q})$ for $U_d = 4.40$ eV, $T = 20$ meV and $\Lambda_0 = 0.5$ eV. The peak positions are $\mathbf{q} = \mathbf{Q}_s = (\pi - \delta_s, \pi)$ and $(\pi, \pi - \delta_s)$ where $\delta_s \approx 0.31\pi$. (d) The U_d dependencies of $\chi_{\max}^{\text{spin}} [\equiv \chi^{\text{spin}}(\mathbf{Q}_s)]$ given by the RG+cRPA method and by the RPA. The initial spin susceptibility given by the cRPA is also shown. No “constrained VC” discussed in Ref. [58] is included in the present RG+cRPA study.

to Y- and Bi-based cuprates by following Ref. [46]. The band filling is set to $n = n_d + n_p = 4.9$, corresponding to the hole filling $x = 0.1$. The FS and the band structure are shown in Figs. 2(a) and 2(b), respectively.

In underdoped cuprates, the spin, charge, and orbital degrees of freedoms are strongly coupled by the electron correlation. This fact had prevented the explanation of the experimentally-observed nematic charge order so far. In order to analyze the competing strong fluctuations in the two-dimensional systems accurately, we apply the RG+cRPA method developed in Refs. [58, 59], in which the \mathbf{q} dependencies of susceptibilities can be obtained with high accuracy in comparison with the conventional patch-RG method.

In the RG+cRPA method proposed in Ref. [58], we set the initial cutoff Λ_0 smaller than the bandwidth [Fig. 2(b)]. The scattering processes of electrons having energies $|E| < \Lambda_0$ are integrated within the one-loop RG scheme based on the conventional N -patch RG method [50–52, 56]. The division of lower-energy Brillouin zone ($|E| < \Lambda_0$) into N_p patches is illustrated in Fig. 2(a). The scattering processes involving higher-energy states with $|E| > \Lambda_0$ are evaluated by the constrained RPA (cRPA) accurately using fine k meshes and incorporated into the initial values. This treatment is based on the natural assumption that the vertex corrections become significant only in the low-energy regions $|E| \ll \Lambda_0$. Due to this treatment, low numerical accuracy for the higher-energy

processes inherent in the conventional patch-RG method is greatly improved in the RG+cRPA method. Another advantage of the RG+cRPA theory for multi-orbital systems is that the inter-band processes (so-called van Vleck contributions) can be included. Therefore, the susceptibilities at low temperatures are obtained with high accuracy in the RG+cRPA method.

In the present analysis we set $\Lambda_0 = 0.5$ eV and $N_p = 128$. We have checked the case for $\Lambda_0 = 1.0$ eV and find that the results are essentially independent of Λ_0 . In the present RG+cRPA method, the numerical accuracy is sufficiently improved in comparison with the conventional patch-RG method. However, the main results of this paper are robust and reproduced qualitatively even in the conventional patch-RG method. The direct comparison between the numerical results of the RG+cRPA and those of the conventional patch-RG method are made in Appendix A.

III. NUMERICAL RESULTS

A. Spin susceptibility

First, we analyze the spin susceptibility using the RG+cRPA method, by following the procedure explained in Refs. [58, 59]. Because of the d -orbital Coulomb interaction U_d , the spin fluctuations develop only on the d orbital. The

d-orbital spin susceptibility per spin is given as

$$\chi^{\text{spin}}(\mathbf{q}) = \frac{1}{2} \int_0^{1/T} d\tau \langle S_d(\mathbf{q}, \tau) S_d(-\mathbf{q}, 0) \rangle, \quad (2)$$

where $S_d(\mathbf{q}, \tau)$ is the spin operator for the *d* orbital. The momentum dependence of the obtained $\chi^{\text{spin}}(\mathbf{q})$ is shown in Fig. 2(c). The strong spin fluctuations are realized at the incommensurate wave vectors $\mathbf{Q}_s = (\pi - \delta_s, \pi)$ and $(\pi, \pi - \delta_s)$. The obtained \mathbf{q} dependence of $\chi^{\text{spin}}(\mathbf{q})$ is consistent with the neutron measurements. As increasing U_d , the maximum of the spin susceptibility, $\chi_{\max}^{\text{spin}}$, develops monotonically and diverges at $U_d = U_d^{\text{cr}} (\approx 4.5 \text{ eV})$, as shown in Fig. 2(d). The value of U_d^{cr} will increase to the first-principles value $U_d \approx 8 \text{ eV}$ by including the spin fluctuation-induced self-energy [66].

As seen from Figs. 2(c) and 2(d), the contributions from the cRPA are small for $\Lambda_0 = 0.5 \text{ eV}$ but quite important (especially for the four-point vertex [58, 59]) in order to derive reliable results. In order to verify the validity of the RG+cRPA theory, we analyzed the same *d*-*p* model by using the conventional patch-RG method established in literature [50–52, 56] in Appendix A: It is confirmed that the essential results given by the RG+cRPA method presented in the main text are *qualitatively* reproduced by the conventional patch-RG method, whereas the numerical accuracy is well improved in the RG+cRPA method.

B. *p*-ODW susceptibility and *d*-orbital BDW susceptibility

In contrast to spin susceptibility, any charge susceptibilities are not enhanced by U_d in the mean-field-level approximations. Nonetheless, we reveal that the strong *p*-ODW instability emerges in the present RG analysis, thanks to the VCs that are dropped in the RPA. Since $U_p = 0$, the effective interaction on *p* orbitals that causes the *p*-ODW instability is originated from the many-body effects on the *d* orbital. The *p*-ODW susceptibility per spin is defined as

$$\chi_{\alpha\beta}^{\text{p-orb}}(\mathbf{q}) = \frac{1}{2} \int_0^{1/T} d\tau \langle n_\alpha(\mathbf{q}, \tau) n_\beta(-\mathbf{q}, 0) \rangle, \quad (3)$$

where $\alpha, \beta = x, y$ represent the p_x, p_y orbitals. According to the experimental analyses [12, 17], we introduce the susceptibilities for the *p*-ODW with *d* and *s'* symmetries:

$$\chi_d^{\text{p-orb}}(\mathbf{q}) \equiv \chi_{xx}^{\text{p-orb}}(\mathbf{q}) + \chi_{yy}^{\text{p-orb}}(\mathbf{q}) - 2\chi_{xy}^{\text{p-orb}}(\mathbf{q}), \quad (4)$$

$$\chi_{s'}^{\text{p-orb}}(\mathbf{q}) \equiv \chi_{xx}^{\text{p-orb}}(\mathbf{q}) + \chi_{yy}^{\text{p-orb}}(\mathbf{q}) + 2\chi_{xy}^{\text{p-orb}}(\mathbf{q}). \quad (5)$$

The susceptibility $\chi_d^{\text{p-orb}}(\mathbf{q})$ measures the development of the antiphase correlation between p_x and p_y orbitals in the same unit cell. Aside from the conventional charge/orbital orders, it was pointed out in literature [28–30, 33, 35, 63] that the bond-density order with *d*-wave form factor is expected to develop in the Hubbard model. Therefore, we calculate the *d*-orbital BDW susceptibility:

$$\chi^{\text{BDW}}(\mathbf{q}) = \frac{1}{2} \int_0^{1/T} d\tau \langle B(\mathbf{q}, \tau) B(-\mathbf{q}, 0) \rangle, \quad (6)$$

$$B(\mathbf{q}) = \sum_{\mathbf{k}, \sigma} f(\mathbf{k} + \mathbf{q}/2) d_{\mathbf{k}, \sigma}^\dagger d_{\mathbf{k} + \mathbf{q}, \sigma}, \quad (7)$$

where $f(\mathbf{k})$ is the *d*-wave form factor: $f(\mathbf{k}) = \cos(k_x) - \cos(k_y)$. The order parameter $\langle B(\mathbf{q}) \rangle \neq 0$ represents the bond-ordered state, which is equivalent to the modulation of the hopping integrals [35]. In the case of $\mathbf{q} = \mathbf{0}$, the susceptibility $\chi^{\text{BDW}}(\mathbf{q} = \mathbf{0})$ measures the nematic or Pomeranchuk instability [50–52, 56]. We also evaluate the conventional *d*-orbital charge susceptibility

$$\chi^{\text{d-orb}}(\mathbf{q}) = \frac{1}{2} \int_0^{1/T} d\tau \langle n_d(\mathbf{q}, \tau) n_d(-\mathbf{q}, 0) \rangle, \quad (8)$$

where $n_d(\mathbf{q}, \tau)$ is the density operator for the *d* orbital. Although the upper limit of $\chi^{\text{d-orb}}(\mathbf{q})$ is $1/U_d$ in the present Hubbard model, $\chi^{\text{d-orb}}(\mathbf{q})$ in the one-loop RG may diverge unphysically if we set U_d too large. Thus, we always verify the non-singular behavior of $\chi^{\text{d-orb}}(\mathbf{q})$ to ensure that the adopted parameter value is within a valid range. We applied the finite-temperature RG formalism based on the sharp bandwidth cutoff and solved the RG equations down to $\Lambda_l = 0$. In the actual calculation of the RG equations, we introduce a lower-energy cutoff $\Lambda_l = \pi T$ for the four-point vertex function in order to obtain stable numerical results [31]. The physical meaning of this lower-energy cutoff is, for example, the suppression of the Cooper channel due to the impurity scattering or the magnetic field. Experimentally, the charge-density-wave state is strongly stabilized by applying the magnetic field beyond 15 T [67, 68]. This fact means that the Cooper instability is less important for the density-wave-formation mechanism.

In Fig. 3, we present the obtained *p*-ODW susceptibilities with *d* and *s'* symmetries, together with the *d*-orbital BDW susceptibility for $U_d = 4.40 \text{ eV}$ in (a)-(d), and $U_d = 4.50 \text{ eV}$ in (e)-(h). In the case of $U_d = 4.40 \text{ eV}$, in which the spin susceptibility is moderate ($\chi_{\max}^{\text{spin}} \approx 12 \text{ eV}^{-1}$), both $\chi_d^{\text{p-orb}}$ and χ^{BDW} are enlarged compared to the RPA results as shown in Figs. 3(a) and 3(c), whereas $\chi_{s'}^{\text{p-orb}}$ in Fig. 3(b) is not enhanced at all. Therefore, the *p*-ODW and BDW susceptibilities are moderately enhanced by the VCs that are neglected in the RPA. However, the highest peaks of both $\chi_d^{\text{p-orb}}$ and χ^{BDW} are located at $\mathbf{q} = \mathbf{Q}_d$, inconsistently with the axial nematic density wave in cuprates.

In the case of $U_d = 4.50 \text{ eV}$, in which the spin susceptibility is large ($\chi_{\max}^{\text{spin}} \approx 200 \text{ eV}^{-1}$), both the *p*-ODW and *d*-orbital BDW susceptibilities shown in Figs. 3(e) and 3(g) possess large sharp peaks at $\mathbf{q} = \mathbf{Q}_a$ and \mathbf{Q}_d , which originate from the VCs generated in the renormalization procedure. The most divergent density-wave susceptibility is $\chi_d^{\text{p-orb}}(\mathbf{q})$ at $\mathbf{q} = \mathbf{Q}_a$. In contrast, $\chi_{s'}^{\text{p-orb}}(\mathbf{q})$ is seldom enhanced. Therefore, the axial *p*-ODW with *d* symmetry shown in Fig. 1(a) is realized. We have verified that $|\mathbf{Q}_a| = \delta_a$ increases with hole doping in the present RG study, consistently with experiments in the Y-, Bi-, and Hg-based compounds. According to neutron inelastic scattering studies, $\chi_{\max}^{\text{spin}}$ is as large as $\sim 500 \text{ eV}^{-1}$ in the slightly underdoped YBCO [69]. Therefore, the nematic density wave in cuprates is realized in the strong-spin fluctuation region experimentally.

We note that both $\chi_d^{\text{p-orb}}$ and χ^{BDW} have sub-dominant broad peaks at $\mathbf{q} = \mathbf{0}$, indicating that “the $\mathbf{q} = \mathbf{0}$ Pomer-

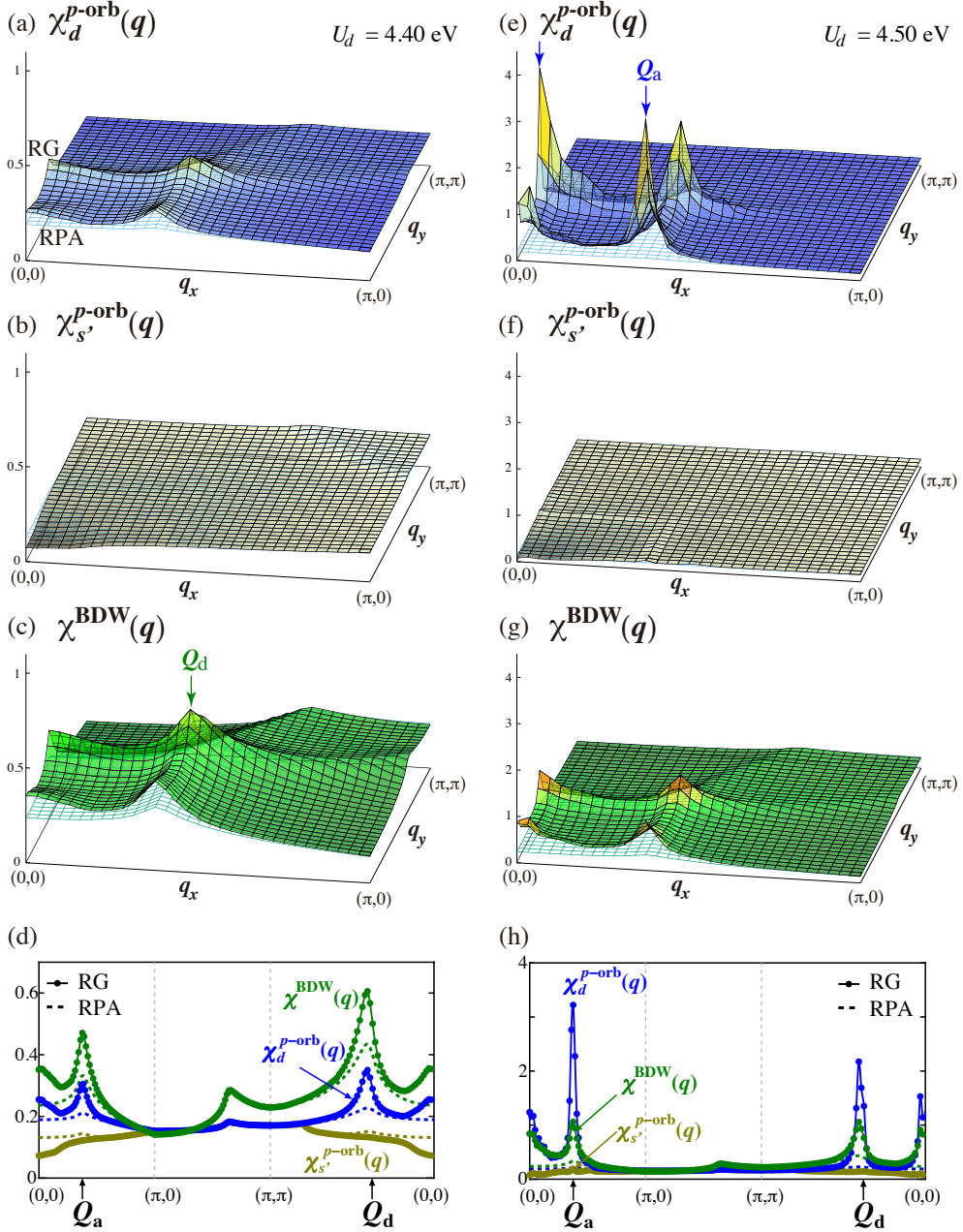


FIG. 3. The p -ODW [$\chi_d^{p\text{-orb}}(\mathbf{q})$ and $\chi_{s'}^{p\text{-orb}}(\mathbf{q})$] and d -orbital BDW [$\chi^{\text{BDW}}(\mathbf{q})$] susceptibilities in the three-orbital Hubbard model with $U_d = 4.40$ eV in (a)-(d), and $U_d = 4.50$ eV in (e)-(h). The temperature is $T = 20$ meV. The maximum of the spin susceptibility is $\chi_{\max}^{\text{spin}} \approx 12$ eV $^{-1}$ (200 eV $^{-1}$) for $U_d = 4.40$ eV (4.50 eV). The RPA results are also shown for comparison. The axial wave vector is $Q_a \approx (0.37\pi, 0)$ and the diagonal wave vector is $Q_d \approx (0.41\pi, 0.41\pi)$. Both peak positions Q_a and Q_d correspond to the wave vector connecting the hot spots shown in Fig. 1(b). The wave vectors Q_a and Q_d obtained from the RG+cRPA method change with carrier doping, by following the change in the vectors connecting the hot spots.

anchuk instabilities” are also enhanced in the present model. This instability had been reported in the previous theoretical studies [31, 70–72], and also observed experimentally in cuprates as the enhancement of the B_{1g} channel Raman response [70–72]. The temperature-flow RG scheme [53] would also be useful for the study of the Pomeranchuk instability [50, 54].

IV. DISCUSSIONS

A. Scaling relation between p -ODW susceptibility and spin susceptibility

In the inset of Fig. 4(a), we show the U_d dependencies of p -ODW and d -orbital BDW susceptibilities at $\mathbf{q} = Q_a$. The p -ODW susceptibility exceeds the BDW one with increasing U_d . In the main figure of Fig. 4(a), we plot both the p -ODW

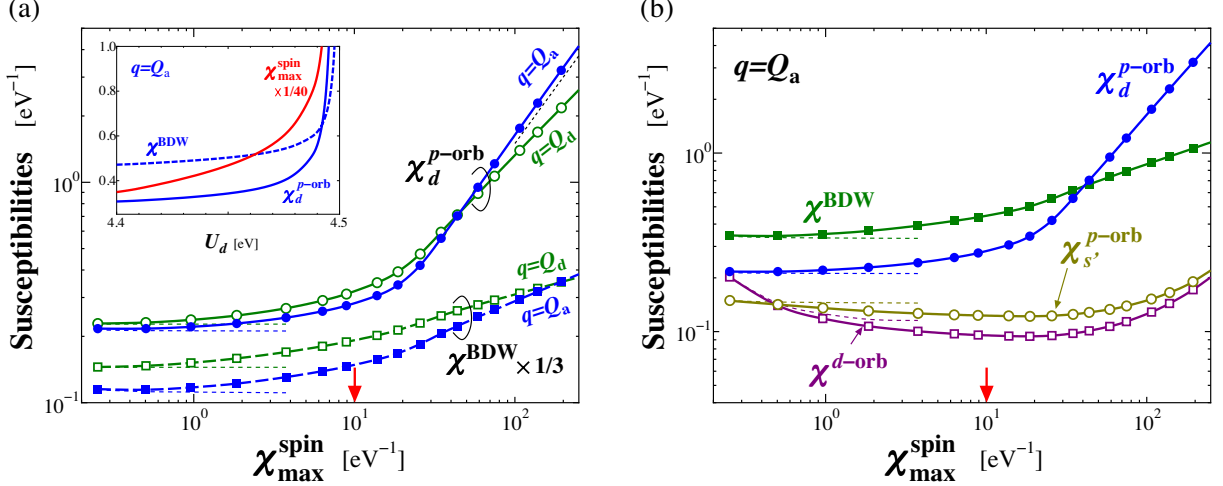


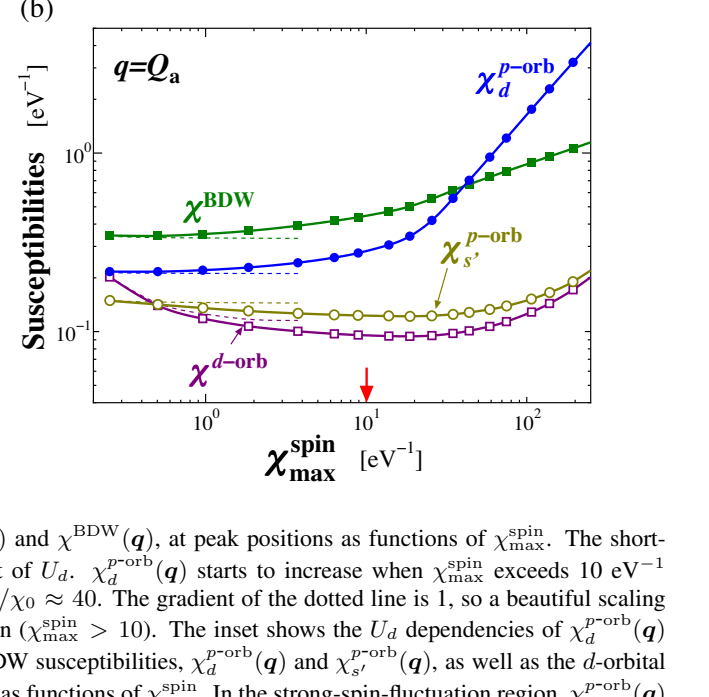
FIG. 4. (a) The p -ODW and d -orbital BDW susceptibilities, $\chi_d^{p\text{-orb}}(\mathbf{q})$ and $\chi^{BDW}(\mathbf{q})$, at peak positions as functions of $\chi_{\max}^{\text{spin}}$. The short-dashed lines represent the RPA results, which are almost independent of U_d . $\chi_d^{p\text{-orb}}(\mathbf{q})$ starts to increase when $\chi_{\max}^{\text{spin}}$ exceeds 10 eV^{-1} (shown by the arrow). The corresponding Stoner enhancement is $\chi_{\max}^{\text{spin}}/\chi_0 \approx 40$. The gradient of the dotted line is 1, so a beautiful scaling relation $\chi_d^{p\text{-orb}} \propto \chi_{\max}^{\text{spin}}$ is satisfied in the strong-spin-fluctuation region ($\chi_{\max}^{\text{spin}} > 10$). The inset shows the U_d dependencies of $\chi_d^{p\text{-orb}}(\mathbf{q})$ and $\chi^{BDW}(\mathbf{q})$ at $\mathbf{q} = \mathbf{Q}_a$. (b) The d -symmetry and s' -symmetry p -ODW susceptibilities, $\chi_d^{p\text{-orb}}(\mathbf{q})$ and $\chi_{s'}^{p\text{-orb}}(\mathbf{q})$, as well as the d -orbital BDW and charge susceptibilities, $\chi^{BDW}(\mathbf{q})$ and $\chi^{d\text{-orb}}(\mathbf{q})$, at $\mathbf{q} = \mathbf{Q}_a$, as functions of $\chi_{\max}^{\text{spin}}$. In the strong-spin-fluctuation region, $\chi_d^{p\text{-orb}}(\mathbf{q})$ exhibits a critical enhancement, whereas the d -orbital charge susceptibility $\chi^{d\text{-orb}}(\mathbf{q})$ remains small. Thus, the enhancement of $\chi_d^{p\text{-orb}}(\mathbf{Q}_a)$ is obtained within the reliable parameter range of the RG method.

and d -orbital BDW susceptibilities at $\mathbf{q} = \mathbf{Q}_a$ and \mathbf{Q}_d as functions of $\chi_{\max}^{\text{spin}}$, in order to reveal the correlation between the spin and density susceptibilities. In the weak-spin-fluctuation region ($\chi_{\max}^{\text{spin}} \lesssim 10 \text{ eV}^{-1}$), both the p -ODW and d -orbital BDW susceptibilities increase moderately. In the strong-spin-fluctuation region, only $\chi_d^{p\text{-orb}}(\mathbf{q})$ starts to increase drastically in proportion to $\chi_{\max}^{\text{spin}}$. In this region, the highest peak of $\chi_d^{p\text{-orb}}(\mathbf{q})$ shifts to $\mathbf{q} = \mathbf{Q}_a$, consistently with the experimental wave vector. The relation $\chi_d^{p\text{-orb}}(\mathbf{Q}_a) \gg \chi^{BDW}(\mathbf{Q}_a)$ is robust against the choice of model parameters.

The most important finding in Fig. 4(a) is that $\chi_d^{p\text{-orb}}(\mathbf{q})$ at $\mathbf{q} = \mathbf{Q}_a$ well scales to $\chi_{\max}^{\text{spin}}$ in the strong-fluctuation region ($\chi_{\max}^{\text{spin}} \gtrsim 10 \text{ eV}^{-1}$). This beautiful scaling relation is obtained in the wide range of model parameters. This fact indicates that the p -ODW is driven by the Aslamazov-Larkin VC that describes the strong interference between spin and orbital fluctuations. Also, as shown in Fig. 4(b), $\chi_{s'}^{p\text{-orb}}(\mathbf{q})$ as well as the conventional charge susceptibility for the d orbital $\chi^{d\text{-orb}}(\mathbf{q})$ decrease with $\chi_{\max}^{\text{spin}}$ in the weak-spin-fluctuation region, whereas they turn to increase slightly in the strong-spin-fluctuation region. The obtained relation $\chi^{d\text{-orb}}(\mathbf{q}) < 1/U_d$ supports the reliability of the present RG result even for $\chi_{\max}^{\text{spin}} \sim 200 \text{ eV}^{-1}$.

B. Why is the axial p -ODW susceptibility enlarged in the strong-spin-fluctuation region?

In order to understand the physical origin of the p -ODW and, in addition, in order to confirm the validity of the present RG analysis, we also perform the diagrammatical analysis for the d - p Hubbard model. Hereafter, we demonstrate that



the characteristic behaviors of the p -ODW and BDW susceptibilities are well understood by taking VCs for the irreducible susceptibilities. The lowest-order Maki-Thompson and Aslamazov-Larkin VCs, $X_{MT}(\mathbf{q})$ and $X_{AL}(\mathbf{q})$, are shown diagrammatically in Fig. 5(a). Their exact expressions are given in Appendix C. In the strong-spin-fluctuation region, the Aslamazov-Larkin VC is scaled as [46]

$$X_{AL}(\mathbf{Q}_a) \propto \sum_{\mathbf{q}} \chi^{\text{spin}}(\mathbf{q}) \chi^{\text{spin}}(\mathbf{q} + \mathbf{Q}_a) \propto \xi^2 \propto \chi_{\max}^{\text{spin}}, \quad (9)$$

where ξ is the magnetic correlation length, while the Maki-Thompson VC is scaled as

$$X_{MT}(\mathbf{Q}_{a,d}) \propto \sum_{\mathbf{q}} \chi^{\text{spin}}(\mathbf{q} + \mathbf{Q}_{a,d}) \propto \ln \xi^2 \propto \ln \chi_{\max}^{\text{spin}}. \quad (10)$$

Thus, the Aslamazov-Larkin VC is expected to dominate over the Maki-Thompson VC in the strong-spin-fluctuation region.

Figure 5(b) shows the \mathbf{q} dependencies of the Maki-Thompson and Aslamazov-Larkin VCs for the p -ODW susceptibility, at $U_d = 4.06 \text{ eV}$ and $T = 50 \text{ meV}$. In this case, the system is in the intermediate-spin-fluctuation region with $\chi_{\max}^{\text{spin}} \approx 24 \text{ eV}^{-1}$. Here the Aslamazov-Larkin VC possesses the highest peak at $\mathbf{q} = \mathbf{Q}_a$, and the Maki-Thompson VC has the second highest peak at $\mathbf{q} = \mathbf{Q}_d$. Thus, the irreducible susceptibility

$$\Phi_d^{p\text{-orb}}(\mathbf{q}) \equiv \chi_{d,0}^{p\text{-orb}}(\mathbf{q}) + X_{d,MT}^{p\text{-orb}}(\mathbf{q}) + X_{d,AL}^{p\text{-orb}}(\mathbf{q}) \quad (11)$$

has the largest peak at $\mathbf{q} = \mathbf{Q}_a$ due to the Aslamazov-Larkin VC.

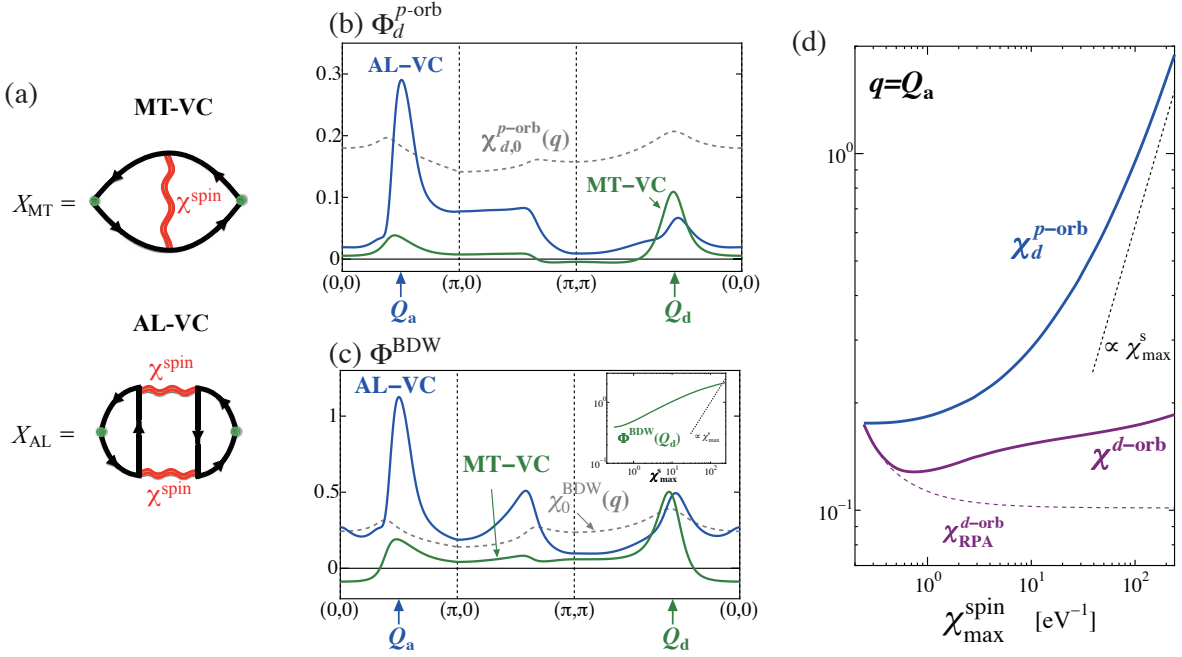


FIG. 5. (a) The lowest-order Maki-Thompson VC $X_{\text{MT}}(\mathbf{q})$ and Aslamazov-Larkin VC $X_{\text{AL}}(\mathbf{q})$. Their exact mathematical expressions are given in Appendix C. (b) The momentum dependencies of the Maki-Thompson and Aslamazov-Larkin VCs for the p -ODW susceptibility, at $T = 50$ meV. The magnitude of U_d is set to satisfy the Stoner factor $\alpha_s = 0.99$. The noninteracting susceptibility $\chi_{d,0}^{p\text{-orb}}(\mathbf{q})$ is also shown. (c) The Maki-Thompson and Aslamazov-Larkin VCs for the d -orbital BDW susceptibility, for $\alpha_s = 0.99$ with $T = 50$ meV. At $\mathbf{q} = \mathbf{Q}_d$, the Maki-Thompson and Aslamazov-Larkin VCs are comparable. The inset shows that $\Phi_{\text{BDW}}(\mathbf{Q}_d)$ does not scale to $\chi_{\max}^{\text{spin}}$. (d) The full susceptibilities $\chi_d^{p\text{-orb}}(\mathbf{Q}_a)$ and $\chi_d^{d\text{-orb}}(\mathbf{Q}_a)$ as functions of $\chi_{\max}^{\text{spin}}$. The scaling relation $\chi_d^{p\text{-orb}}(\mathbf{Q}_a) \propto \chi_{\max}^{\text{spin}}$ is well satisfied in the strong-spin-fluctuation region. For comparison, the RPA result for $\chi_d^{d\text{-orb}}(\mathbf{Q}_a)$ is also shown.

We also show the Maki-Thompson and Aslamazov-Larkin VCs for the d -orbital BDW susceptibility in Fig. 5(c). Since both VCs have large peaks at $\mathbf{q} = \mathbf{Q}_d$, the irreducible susceptibility

$$\Phi^{\text{BDW}}(\mathbf{q}) \equiv \chi_0^{\text{BDW}}(\mathbf{q}) + X_{\text{MT}}^{\text{BDW}}(\mathbf{q}) + X_{\text{AL}}^{\text{BDW}}(\mathbf{q}) \quad (12)$$

takes the highest peak at $\mathbf{q} = \mathbf{Q}_d$. As shown in the inset of Fig. 5(c), $\Phi^{\text{BDW}}(\mathbf{q})$ at $\mathbf{q} = \mathbf{Q}_d$ does not scale to $\chi_{\max}^{\text{spin}}$, which is consistent with the smallness of $\chi^{\text{BDW}}(\mathbf{q})$ in Fig. 4(a).

Next, we derive the full susceptibilities from the irreducible susceptibilities. Figure 5(d) shows the obtained $\chi_d^{p\text{-orb}}(\mathbf{q})$ and $\chi_d^{d\text{-orb}}(\mathbf{q})$ at $\mathbf{q} = \mathbf{Q}_a$ as functions of $\chi_{\max}^{\text{spin}}$ by changing U_d . Since $U_p = 0$ in the present model, the p -ODW susceptibility is well approximated as $\chi_d^{p\text{-orb}}(\mathbf{q}) \approx \Phi_d^{p\text{-orb}}(\mathbf{q})$. The obtained $\chi_d^{p\text{-orb}}(\mathbf{Q}_a)$ behaves very similarly to the RG result in Fig. 4(a). Especially, the scaling relation $\chi_d^{p\text{-orb}}(\mathbf{Q}_a) \propto \chi_{\max}^{\text{spin}}$ is well reproduced by the diagrammatic analysis, due to large contribution from the Aslamazov-Larkin VC. In contrast, the d -orbital charge susceptibility

$$\chi^{d\text{-orb}}(\mathbf{q}) = \frac{\Phi^{d\text{-orb}}(\mathbf{q})}{1 + U_d \Phi^{d\text{-orb}}(\mathbf{q})}, \quad (13)$$

at $\mathbf{q} = \mathbf{Q}_a$ shows a minimum at finite $\chi_{\max}^{\text{spin}}$, similarly to the RG result in Fig. 4(b). This behavior is also understood analytically: In the weak-spin-fluctuation region, in which

the VCs are negligible and therefore $\Phi^{d\text{-orb}}(\mathbf{q}) \approx \chi_0^{d\text{-orb}}(\mathbf{q})$ is satisfied, the d -orbital susceptibility decreases with U_d in proportion to $1/[1 + U_d \chi_0^{d\text{-orb}}(\mathbf{q})]$. In the strong-spin-fluctuation region, $\Phi^{d\text{-orb}}(\mathbf{q})$ increases drastically because of the Aslamazov-Larkin VC, and therefore $\chi^{d\text{-orb}}(\mathbf{q})$ increases toward $1/U_d$.

Thus, we revealed that the characteristic behaviors of the p -ODW susceptibility in the present RG study, such as the peak position at $\mathbf{q} = \mathbf{Q}_a$ and the scaling relation $\chi_d^{p\text{-orb}}(\mathbf{Q}_a) \propto \chi_{\max}^{\text{spin}}$, are qualitatively understood by including the Aslamazov-Larkin VC into the RPA. This result is never trivial in that the higher-order VCs, unrestricted to the Maki-Thompson and Aslamazov-Larkin VCs, are systematically produced in the RG theory. For example, the higher-order Maki-Thompson and Aslamazov-Larkin processes are included in the RG. Also, the spin and charge fluctuations and the four-point VCs are calculated consistently. Thus, the dominant role of the lowest-order Aslamazov-Larkin VC shown in Fig. 5 is confirmed in the present RG theory.

Of course, the lowest-order Aslamazov-Larkin VC study cannot explain the RG results in many parts. For example, if only the lowest-order Aslamazov-Larkin VC is included, the relation $\chi^{\text{BDW}}(\mathbf{Q}_a) \propto \chi_{\max}^{\text{spin}}$ is realized although it remains small in the RG results. Also, the d -symmetry form factor in the p -ODW cannot simply be obtained by the lowest-order Aslamazov-Larkin VC. These facts indicate the importance of the higher-order diagrams included in the RG.

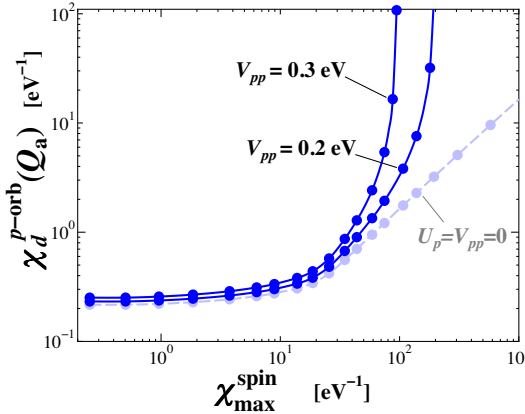


FIG. 6. The p -ODW susceptibility $\chi_d^{p\text{-orb}}(\mathbf{Q}_a; U_p, V_{pp})$ [Eq. (14)] as a function of $\chi_{\max}^{\text{spin}}$ for $U_p = 0.7$ eV. As an approximation, the irreducible susceptibility is given by the RG result for $U_p = V_{pp} = 0$.

Note that there is another type of the Aslamazov-Larkin VC given by the product of spin and charge (or orbital) propagators $\sim \chi^{\text{spin}}(\mathbf{q}') \chi^{\text{charge}}(\mathbf{q}'')$. This gives rise to the correction to the spin susceptibility χ^{spin} and is also included in the present RG formalism. From the data of spin susceptibility [Fig. 2(d)], it can be confirmed that such a VC does not have a strong effect.

C. Effect of the Coulomb interactions for O sites on the p -ODW susceptibility

The scaling relation $\chi_d^{p\text{-orb}}(\mathbf{Q}_a) \propto \chi_{\max}^{\text{spin}}$ obtained in Fig. 4 indicates that the spin-density-wave order and the p -ODW order emerge simultaneously. However, the p -ODW will be realized in the paramagnetic state in the presence of small but finite Coulomb interaction between the nearest-neighbor p - p orbitals, V_{pp} . The p -ODW susceptibility is given as

$$\hat{\chi}^{p\text{-orb}}(\mathbf{q}; U_p, V_{pp}) = \frac{\hat{\chi}^{p\text{-orb}}(\mathbf{q})}{1 + \hat{V}(\mathbf{q}) \hat{\chi}^{p\text{-orb}}(\mathbf{q})}, \quad (14)$$

where $\hat{\chi}^{p\text{-orb}}(\mathbf{q})$ represents the irreducible susceptibility with respect to U_p (the p -orbital onsite interaction) and V_{pp} . The non-zero matrix elements of $\hat{V}(\mathbf{q})$ are $V_{xx} = V_{yy} = U_p$ and $V_{xy} = V_{yx} = 8V_{pp} \cos(q_x/2) \cos(q_y/2)$. When U_p, V_{pp} are very small, $\hat{\chi}^{p\text{-orb}}(\mathbf{q})$ is safely approximated by the RG susceptibility for $U_p = V_{pp} = 0$. Figure 6 shows the obtained $\chi_d^{p\text{-orb}}(\mathbf{Q}_a; U_p, V_{pp})$ for $V_{pp} = 0.2$ and 0.3 eV with $U_p = 0.7$ eV, which diverges even when $\chi_{\max}^{\text{spin}}$ is finite. Now, we explain why the tiny V_{pp} critically enhances the p -ODW susceptibility. Considering the relation $\chi_{xx}^{p\text{-orb}} \chi_{yy}^{p\text{-orb}} \approx [\chi_{xy}^{p\text{-orb}}]^2$ obtained in the present RG at $\mathbf{q} = \mathbf{Q}_a$, the d -symmetry p -ODW susceptibility is approximately given as

$$\chi_d^{p\text{-orb}}(\mathbf{Q}_a; U_p, V_{pp}) \approx \frac{\chi_d^{p\text{-orb}}(\mathbf{Q}_a)}{1 + U_p [\chi_{xx}^{p\text{-orb}}(\mathbf{Q}_a) + \chi_{yy}^{p\text{-orb}}(\mathbf{Q}_a)] + 2V_{xy}(\mathbf{Q}_a) \chi_{xy}^{p\text{-orb}}(\mathbf{Q}_a)}, \quad (15)$$

which is enhanced by V_{pp} since $\chi_{xy}^{p\text{-orb}}(\mathbf{Q}_a)$ is negative. The enhancement due to V_{pp} dominates over the suppression due to U_p , if $U_p \lesssim 8V_{pp} \cos \delta_a$. In real materials, finite electron-phonon coupling would also enlarge the p -ODW susceptibility in the strong-spin-fluctuation region. Therefore, the Aslamazov-Larkin VC accounts for the p -ODW ordering in the pseudogap region of the cuprate superconductors.

V. CONCLUSIONS

In this paper we applied the RG+cRPA theory to the three-orbital d - p Hubbard model and discovered that the d -symmetry p -ODW susceptibility critically develops at $\mathbf{q} = \mathbf{Q}_a$ in the strong-spin-fluctuation region. The main result is shown in Figs. 3(e)–3(h). The obtained p -ODW state has the characteristics: (i) the ordering vector is axial type $\mathbf{Q}_a = (\delta_a, 0)$, (ii) the charge modulation occurs on the oxygen p orbital, and (iii) the symmetry of the p -orbital order pattern is of the d -wave type. Therefore, the present RG+cRPA theory reproduced satisfactorily the experimental charge-density-wave state. The p -ODW originates from the strong interference between the spin and orbital susceptibilities. Such an interference is the main characteristic of the electronic states in underdoped cuprates.

In the previous scenarios of the spin-fluctuation-driven density-wave states, such as BDW [28–37], PDW [38–42], and the composite orders [43, 44], the Maki-Thompson VC has been studied as possible origins [28–30, 33, 36, 41–43]. In the weak-spin-fluctuation region, the Maki-Thompson VC is dominant and the BDW instability with $\mathbf{q} = \mathbf{Q}_d$ is obtained, consistently with Refs. [28–31, 33, 36, 37]. However, in the strong-spin-fluctuation region, the p -ODW with the axial wave vector \mathbf{Q}_a is critically enhanced: The obtained beautiful scaling between the spin and p -ODW susceptibilities means the important role of the Aslamazov-Larkin VC. Therefore, the p -ODW in cuprates originates from the strong interference between the spin and orbital fluctuations, which is microscopically described as the vertex corrections.

Despite that the p -ODW and the d -orbital BDW have the same d symmetry, we found that the p -ODW susceptibility is strongly enhanced while the enhancement of the BDW susceptibility is moderate, as seen from Fig. 4(a). This fact implies that the charge-density modulation in cuprates is not due to the bond modulation of the d orbital, but due to the charge modulation on the p orbital. In fact, the recent x-ray diffraction study reported that the sizable oxygen-site displacements occur in the charge-density-wave state, whereas the Cu-site displacements are very small [73]. This result supports the

p-ODW scenario proposed in this paper.

The RG+cRPA theory developed in this study will be useful for analyzing unsolved problems in strongly-correlated electron systems. For example, it is interesting to apply the RG+cRPA theory for Fe-based superconductors in order to understand the origin of the electronic nematic state [74–77].

ACKNOWLEDGMENTS

The authors are grateful for fruitful discussions with A.V. Chubukov, J.C.S. Davis, K. Fujita, T. Hanaguri, C. Honerkamp, W. Metzner, and S. Onari. This work was supported by Grant-in-Aid for Scientific Research from the Ministry of Education, Culture, Sports, Science, and Technology, Japan.

Appendix A: COMPARISON BETWEEN RG+cRPA AND THE CONVENTIONAL PATCH-RG SCHEME

In the main text, we have analyzed the susceptibilities using the recently developed RG+cRPA theory [58, 59]. In the conventional patch-RG method, the numerical accuracy for the higher-energy processes becomes worse because of the large patch radius [50–52, 56]. In order to improve the numerical accuracy, in the RG+cRPA method, the higher-energy processes are calculated accurately within the cRPA by introducing fine k meshes. For this reason, the q dependences of susceptibilities are obtained very accurately. Although the effect of VCs is underestimated in the RG+cRPA method, this underestimation is not serious since the VCs are important mainly in the lower-energy processes. In this section, we make a direct comparison between the numerical results of the RG+cRPA and those of the conventional patch-RG method in order to confirm the validity and reliability of the RG+cRPA theory.

The band structure and the patch discretization in the conventional patch-RG method are shown in Figs. 7(a) and 7(b), respectively. The Brillouin zone is divided into the patch segments with respect to the angle ϕ_i [Fig. 7(b)]. Here, the radial variable k_r from the center of each patch, $p(\phi_i)$, is neglected in the vertices, that is, $\Gamma(\{k_i\}) = \Gamma(\{k_{r,i}, \phi_i\}) \rightarrow \Gamma(\{\phi_i\})$

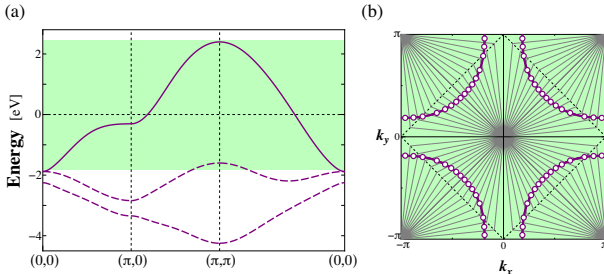


FIG. 7. (a) Band structure and (b) Fermi surface in the present model. The discretization of the Brillouin zone ($N_p = 64$) in the conventional patch-RG scheme are shown. In each patch, the center momentum $p(\phi_i)$ is shown as the open circle. The initial cutoff Λ_0 is set to the bandwidth of the conduction band, and the contributions from the valence bands are neglected.

$$\frac{d}{dl} \frac{k_1 + q}{q} = \sum_{k_2} \frac{k_2}{q} \Gamma(q; \phi_1, \phi'_1) \quad R(q; \phi_1, \phi'_1)$$

$$\frac{d}{dl} \frac{k_1 + q}{q} = \sum_{k_2} \frac{k_2}{q} \Gamma(q; \phi_2, \phi'_2) \quad R(q; \phi_2, \phi'_2)$$

$$\frac{d}{dl} \frac{k_1 + q}{q} = \sum_{k_2} \frac{k_2}{q} \Gamma(\phi_1, \phi'_1; \phi'_2, \phi_2) \quad \Gamma(\phi_1, \phi'_1; \phi'_2, \phi_2)$$

FIG. 8. The RG equations for the three-point vertex $R(q; \phi, \phi')$, where ϕ is the patch index and l is the scaling parameter. The slashed (crossed) line represents an electron propagation having energy on $\Lambda_{l+dl} < |E| < \Lambda_l$ ($|E| > \Lambda_l$) where $\Lambda_l = \Lambda_0 e^{-l}$. The patch indices are determined so that the momenta k_i and $k_i + q$ ($i = 1, 2$) are respectively on the ϕ_i and ϕ'_i patches. Therefore, $k_i \neq p(\phi_i)$ and $k_i + q \neq p(\phi'_i)$.

for the four-point vertex and $R(q; k_1, k_2) \rightarrow R(q; \phi_1, \phi_2)$ for the three-point vertex [50–52, 56]. The justification of this approximation is frequently ascribed to the simple scaling argument in the weak-coupling limit. However, the k_r dependencies are *quantitatively* important in reality, since the “momentum mismatch” problem is serious in the higher-energy processes. Moreover, this problem becomes more serious in multi-orbital systems, since the orbital components of each band, called the “orbital makeup” [56], depend on k_r in usual multi-orbital models.

The conventional patch-RG scheme can be reproduced in the present RG+cRPA method by neglecting the valence-band contributions and by setting the cutoff Λ_0 to the bandwidth of the conduction band [see Fig. 7(a)]. The RG equation for $R(q; \phi_1, \phi_2)$ is shown diagrammatically in Fig. 8. The susceptibilities $\chi^{\text{spin}}(q)$, $\chi_d^{\text{p-orb}}(q)$, $\chi^{\text{BDW}}(q)$, $\chi_{s'}^{\text{p-orb}}(q)$, and $\chi^{\text{d-orb}}(q)$ obtained by the conventional patch-RG method for $U_d = 9.5$ eV are shown in Fig. 9. As shown in Fig. 9(a), strong antiferromagnetic fluctuations are obtained, although the obtained incommensurate peak position of $\chi^{\text{spin}}(q)$ is at $q = (\pi - \delta_s, \pi - \delta_s)$, differently from the experimental peak positions at $q = (\pi, \pi - \delta_s)$ and $(\pi - \delta_s, \pi)$ that are reproduced by the RPA as well as the RG+cRPA theory [see Fig. 2(c)].

Figure 10 shows the inverse of the spin susceptibilities $[\chi^{\text{spin}}(q)]_{\text{RG+cRPA}}$ and $[\chi^{\text{spin}}(q)]_{\text{conv-RG}}$, obtained in the RG+cRPA and conventional patch-RG methods, respectively. In the case of $U_d \sim 0$, $[\chi^{\text{spin}}(q)]_{\text{RG+cRPA}}$ almost perfectly reproduces the RPA susceptibility $\chi^{\text{spin}}_{\text{RPA}}(q) = \chi^0(q)/(1 - U\chi^0(q))$, where $\chi^0(q)$ is the bare susceptibility. It is noteworthy that the result of the RG+cRPA method for $\Lambda_0 = 0.5$ eV is very similar to that for $\Lambda_0 = 1.0$ eV. In contrast, $[\chi^{\text{spin}}(q)]_{\text{conv-RG}}$ gives under-estimated value since the van Vleck contribution is dropped. In addition, $[\chi^{\text{spin}}(q)]_{\text{conv-RG}}$ also deviates from the RPA restricted to the conduction-band contribution, $\chi^{\text{spin}}_{\text{RPA,cond}}(q)$. The origin of this deviation is that the orbital components, called the “orbital makeup” [56, 78], largely depend on k_r because of the large patch radius in the conventional patch-RG method. Thus, the RG+cRPA method is superior to the conventional patch-RG method in the numerically accuracy for $U_d \sim 0$.

Next, we compare the results of two RG methods for finite U_d . As shown in Fig. 10, each $1/[\chi^{\text{spin}}(q)]_{\text{RG+cRPA}}$ and

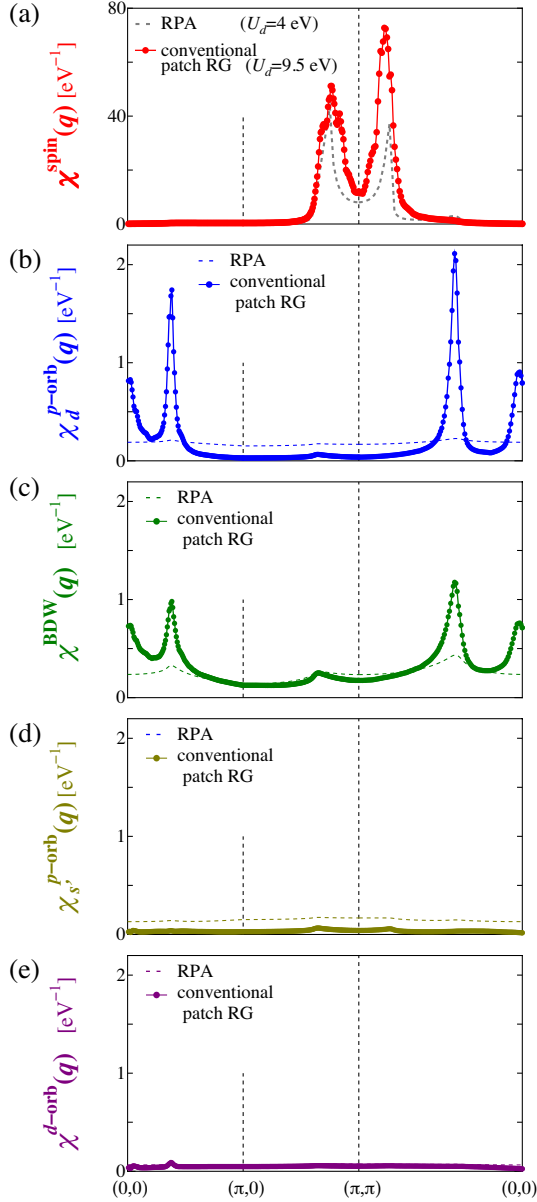


FIG. 9. (a) $\chi^{\text{spin}}(\mathbf{q})$, (b) $\chi_d^{\text{p-orb}}(\mathbf{q})$, (c) $\chi^{\text{BDW}}(\mathbf{q})$, (d) $\chi_{s'}^{\text{p-orb}}(\mathbf{q})$, and (e) $\chi_{d'}^{\text{p-orb}}(\mathbf{q})$, obtained by the conventional patch-RG method. We set $U_d = 9.5$ eV, $T = 20$ meV, and $N_p = 64$. For comparison, the RPA result for $\chi^{\text{spin}}(\mathbf{q})$ with $U_d = 4$ eV is also shown in (a), and the RPA results for $U_d = 9.5$ eV are shown in (b)-(e). As shown in (b) and (c), d -symmetry p -ODW instability at $\mathbf{q} = \mathbf{Q}_a$ develops strongly. These results are consistent with the results of the RG+cRPA method explained in the main text.

$1/[\chi^{\text{spin}}(\mathbf{q})]_{\text{conv-RG}}$ is concave as functions of U_d because of the VC generated in the three- and four-point vertices. We see that $U_d^{\text{cr}} \approx 4.5 - 5$ eV in the RG+cRPA method, whereas $U_d^{\text{cr}} \approx 9.5$ eV in the conventional patch-RG method. To understand such large difference in U_d^{cr} , in Fig. 8, we comment on the “momentum mismatch” between the pair of the Green functions $G(\mathbf{k}_2)G(\mathbf{k}_2 + \mathbf{q})$ and Γ, R , originating from the fact that the momenta at the centers of the patches ϕ_2 and

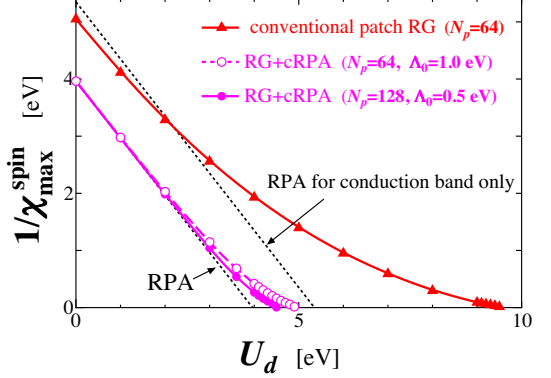


FIG. 10. The U_d dependence of $\chi_{\max}^{\text{spin}}$ obtained by the conventional patch-RG method, RG+cRPA methods, and RPA. In the RG+cRPA, the results with the different choices of parameters are shown. In the weak-coupling limit, the RG+cRPA results well reproduce the RPA results, irrespective to the choice of N_p . In addition, the Λ_0 dependence of the results is weak in the RG+cRPA.

ϕ'_2 , $\mathbf{p}(\phi_2)$ and $\mathbf{p}(\phi'_2)$, are different from \mathbf{k}_2 and $\mathbf{k}_2 + \mathbf{q}$, respectively. This mismatch leads to violation of the momentum conservation at each bare vertex U_d in the Feynman diagrams. This defect is not serious in the RG+cRPA method with $\Lambda_0 \ll W_{\text{band}}$. Considering that the self-energy correction is dropped in the present RG methods, large U_d^{cr} in the conventional patch-RG method might partially originate from the momentum mismatch. On the other hand, U_d^{cr} in the RG+cRPA method is underestimated since the vertex corrections with higher-energy processes ($|E| > \Lambda_0$) are included only partially. In spite of this underestimation, large p -ODW susceptibility is induced by the VC in the RG+cRPA method.

We stress that the results of the RG+cRPA method and those of the conventional patch-RG method are qualitatively equivalent, nonetheless of the large difference in U_d^{cr} . In the RG+cRPA method, the results are almost unchanged in the both cases of $\Lambda_0 = 0.5$ eV and $\Lambda_0 = 1.0$ eV. In addition, the RG+cRPA results with $N_p = 64$ and 128 are almost identical, indicating that the numerical convergence has been achieved at $N_p \approx 64$. We note that various RG methods have been proposed to resolve the above-mentioned problems in the conventional patch-RG method, such as the singular-mode functional renormalization group [78].

Regarding the charge susceptibilities, both $\chi_d^{\text{p-orb}}(\mathbf{q})$ and $\chi^{\text{BDW}}(\mathbf{q})$ possess large sharp peaks at $\mathbf{q} = \mathbf{Q}_a$ and \mathbf{Q}_d as shown in Figs. 9(b) and 9(c) at $U_d = 9.5$ eV. This behavior is essentially identical to that obtained by RG+cRPA method (Fig. 3). This result supports the validity of the present RG+cRPA theory. Since the van Vleck contributions are dropped in the conventional patch-RG method, both $\chi_d^{\text{p-orb}}(\mathbf{q})$ and $\chi_{s'}^{\text{p-orb}}(\mathbf{q})$ in Figs. 9(b) and 9(d) are much smaller than the RPA results except near the peak positions. In the RG+cRPA, in contrast, the RG+cRPA results coincide well with the RPA results if \mathbf{q} is away from the peak positions, as shown in Fig. 3.

Figure 11 shows the scaling relation between the p -ODW susceptibility and $\chi_{\max}^{\text{spin}}$ obtained from the conventional

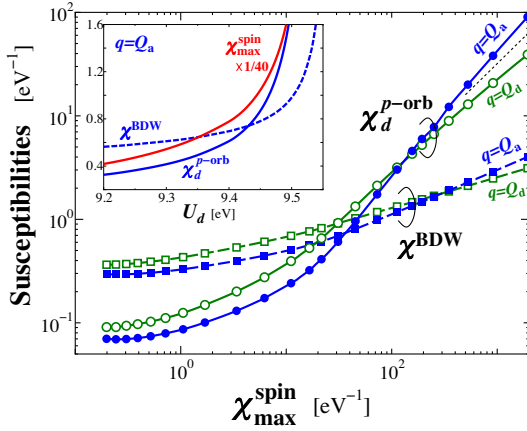


FIG. 11. Peak values of $\chi_d^{p\text{-orb}}(\mathbf{q})$ and $\chi^{\text{BDW}}(\mathbf{q})$ as functions of $\chi_{\max}^{\text{spin}}$ obtained from the conventional patch-RG method. The gradient of the dotted line is 1, so beautiful scaling relation $\chi_d^{p\text{-orb}}(\mathbf{q}) \propto \chi_{\max}^{\text{spin}}$ is satisfied in the strong-coupling regime. The inset shows the U_d dependencies of $\chi_d^{p\text{-orb}}(\mathbf{q})$ and $\chi^{\text{BDW}}(\mathbf{q})$ at $\mathbf{q} = \mathbf{Q}_a$.

patch-RG method. The obtained relations $\chi_d^{p\text{-orb}}(\mathbf{Q}_a) \propto \chi_{\max}^{\text{spin}}$ as well as $\chi_d^{p\text{-orb}}(\mathbf{Q}_a) \gg \chi^{\text{BDW}}(\mathbf{Q}_a)$ in the strong-spin-fluctuation region are qualitatively consistent with the RG+cRPA results shown in Fig. 5. Therefore, the development of the d -symmetry axial p -ODW instability due to the spin fluctuation, which is the main message of the main text derived from the RG+cRPA, is confirmed also by the conventional patch-RG method.

In summary, the results given by the RG+cRPA method presented in the main text are qualitatively reproduced by the conventional patch-RG method. Therefore, the validity of the RG+cRPA method is verified by the conventional patch-RG method, the validity of which has been confirmed in literature [50–52, 56]. The numerical accuracy is well improved in the RG+cRPA method, as recognized by the coincidence with the RPA result in the weak-coupling region shown in Fig. 10. This improvement is achieved by calculating the higher-energy processes accurately within the cRPA by introducing the fine \mathbf{k} meshes. As seen from Figs. 2(c) and 2(d), the contributions from the cRPA are small for $\Lambda_0 = 0.5$ eV but quite important (especially for the four-point vertex [58, 59]) in order to derive reliable results from the RG equations.

Appendix B: SCALING FLOWS OF EFFECTIVE INTERACTIONS

In this section, we examine the effective interactions for p -ODW and d -orbital BDW. The effective interaction for the d -orbital BDW state is given by taking into account the d -form factor

$$\Gamma^{\text{BDW}}(\mathbf{q}) \equiv \sum'_{\mathbf{k}, \mathbf{k}'} \Gamma^c(\mathbf{k}, \mathbf{k}'; \mathbf{k} + \mathbf{q}, \mathbf{k}' - \mathbf{q}) \\ \times u_d^*(\mathbf{k}) u_d^*(\mathbf{k}') u_d(\mathbf{k} + \mathbf{q}) u_d(\mathbf{k}' - \mathbf{q}) \\ \times f(\mathbf{k} + \mathbf{q}/2) f(\mathbf{k}' - \mathbf{q}/2), \quad (\text{B1})$$

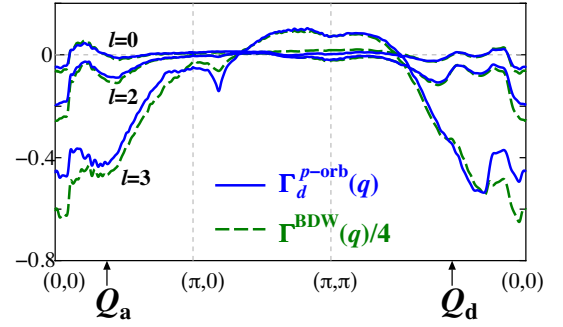


FIG. 12. The effective interactions (B1) and (B2) at the scaling parameter $l = 0, 2$, and 3 , with $U_d = 4.50$ eV, $T = 20$ meV, $N_p = 128$. In this case, $\chi_d^{p\text{-orb}}(\mathbf{Q}_a)$ is larger than $\chi^{\text{BDW}}(\mathbf{Q}_d)$ [see Fig. 3(h)].

where $\Gamma^c(\mathbf{k}, \mathbf{k}'; \mathbf{k} + \mathbf{q}, \mathbf{k}' - \mathbf{q})$ represents the renormalized charge vertex. This expression is essentially the same as examined in the single-orbital case [31]. Here, $u_d(\mathbf{k})$ represents the unitary transformation from the conduction band basis to the d -orbital basis. The summations over \mathbf{k} and \mathbf{k}' are restricted to the low-energy scattering processes, in which all the momenta $(\mathbf{k}, \mathbf{k}', \mathbf{k} + \mathbf{q}, \mathbf{k}' - \mathbf{q})$ are near the Fermi surface. This interaction becomes zero if the bare Hubbard interaction U_d is used for Γ^c [31]. In the present case, $\Gamma^{\text{BDW}}|_{l=0}$ becomes small but nonzero due to the cRPA contributions.

In the similar manner, the effective interaction for the p -ODW state can be introduced as

$$\Gamma_d^{p\text{-orb}}(\mathbf{q}) \equiv \Gamma_{xxx}^c(\mathbf{q}) + \Gamma_{yyy}^c(\mathbf{q}) \\ - \Gamma_{xyxy}^c(\mathbf{q}) - \Gamma_{yxyx}^c(\mathbf{q}), \quad (\text{B2})$$

$$\Gamma_{\alpha\beta\gamma\delta}^c(\mathbf{q}) \equiv \sum'_{\mathbf{k}, \mathbf{k}'} \Gamma^c(\mathbf{k}, \mathbf{k}'; \mathbf{k} + \mathbf{q}, \mathbf{k}' - \mathbf{q}) \\ \times u_\alpha^*(\mathbf{k}) u_\beta^*(\mathbf{k}') u_\gamma(\mathbf{k} + \mathbf{q}) u_\delta(\mathbf{k}' - \mathbf{q}), \quad (\text{B3})$$

where $u_\alpha(\mathbf{k})$ ($\alpha = x, y$) represents the unitary transformation from the band basis to the p_x - or p_y -orbital basis.

As has been discussed in Ref. [31], the negative values of the effective interactions indicate the precursor of the corresponding instability. Actually, if the effective interaction becomes negative, the rhs of the RG equations for the three-point vertex [58] becomes positive and then the three-point vertex can increase. Once the three-point vertex is enhanced, the corresponding susceptibility is also enhanced [58].

In Fig. 12, we show the development of the effective interactions for several scaling parameters $l = \ln(\Lambda_0/\Lambda)$ in the case of $U = 4.50$ eV. At the initial point ($l = 0$), these effective interactions given by the cRPA are small and almost independent of \mathbf{q} . After the renormalization ($l = 2, 3$), the effective interactions at \mathbf{Q}_a and \mathbf{Q}_d become negative, implying the development of the susceptibilities. At $l = 3$, the interaction at $\mathbf{q} = \mathbf{Q}_a$ is stronger than that at $\mathbf{q} = \mathbf{Q}_d$. We find that the overall profile of $\Gamma^{\text{BDW}}(\mathbf{Q}_a)$ is similar to $\Gamma^{p\text{-orb}}(\mathbf{Q}_a)$, except for the constant factor.

In contrast, in the weak-fluctuation case ($U_d = 4.40$ eV), the interaction at $\mathbf{q} = \mathbf{Q}_a$ becomes weaker than that at $\mathbf{q} =$

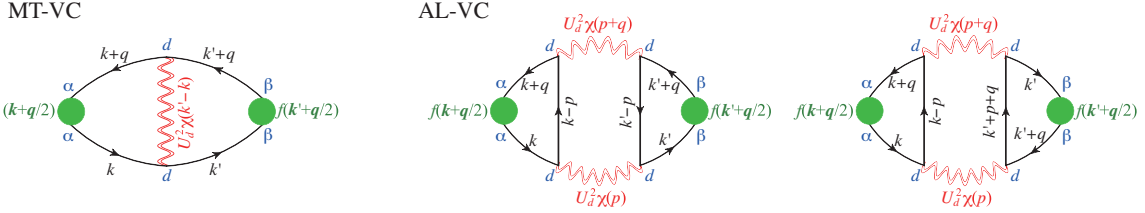


FIG. 13. Detailed diagrammatic expressions of the Maki-Thompson and Aslamazov-Larkin VCs. Their analytic equations are shown in Eqs. (C3)–(C6).

Q_d . This relation of the effective interactions is in accordance with that of the peak positions of the susceptibility.

Thus, we understand that the enhancements of $\chi^{BDW}(\mathbf{q})$ and $\chi_d^{p\text{-orb}}(\mathbf{q})$ at $\mathbf{q} = \mathbf{Q}_a, \mathbf{Q}_d$, and $\mathbf{0}$ originate from the large negative $\Gamma^{BDW}(\mathbf{q})$ and $\Gamma^{p\text{-orb}}(\mathbf{q})$ after the renormalization. However, the \mathbf{q} dependencies of $\Gamma^{BDW}(\mathbf{q})$ and $\Gamma^{p\text{-orb}}(\mathbf{q})$ are not consistent with those of the susceptibilities. For example, the peak position of each $\chi^{BDW}(\mathbf{q})$ and $\chi_d^{p\text{-orb}}(\mathbf{q})$ is $\mathbf{q} = \mathbf{Q}_a$ or \mathbf{Q}_d for $U_d = 4.50$ eV as shown in Figs. 3(e)–3(h), although both $|\Gamma^{BDW}(\mathbf{q})|$ and $|\Gamma^{p\text{-orb}}(\mathbf{q})|$ take the maximum values at $\mathbf{q} = \mathbf{0}$. These results mean that the susceptibilities should be calculated to obtain the real density-wave wave vector in the RG study.

Appendix C: ANALYTICAL EXPRESSIONS OF THE MAKI-THOMPSON AND ASLAMAZOV-LARKIN VERTEX CORRECTIONS

In this section, we show the analytical expressions of the leading-order Aslamazov-Larkin VC $X_{l,m}^{\text{AL}c}(q)$ and Maki-Thompson VC $X_{l,m}^{\text{MT}c}(q)$ for the charge channel, including the form factor $f_\alpha(\mathbf{k})$. The Maki-Thompson VC is given by

$$\begin{aligned} X_{\alpha,\beta}^{\text{MT}c}(q) &= T^2 U_d^2 \sum_{k,k'} f_\alpha\left(\mathbf{k} + \frac{\mathbf{q}}{2}\right) G_{\alpha,d}(k+q) G_{d,\alpha}(k) \\ &\quad \times \left[\frac{3}{2} \chi^{\text{spin}}(k-k') + \frac{1}{2} \chi^{\text{charge}}(k-k') \right] \\ &\quad \times G_{\beta,d}(k') G_{d,\beta}(k'+q) f_\beta\left(k' + \frac{\mathbf{q}}{2}\right), \end{aligned} \quad (\text{C1})$$

where $k = (\mathbf{k}, \epsilon_l)$, $q = (\mathbf{q}, i\omega_m)$, $\epsilon_l = \pi T(2l+1)$, $\omega_m = 2\pi mT$, and $\alpha, \beta = d, x, y$ represent the orbital indices. Here,

χ^{spin} and $\chi^{\text{charge}} (\equiv \chi^{d\text{-orb}})$ represent the d -orbital spin and charge susceptibilities, given by Eqs. (2) and (8), respectively. The Aslamazov-Larkin VC is given by

$$\begin{aligned} X_{\alpha,\beta}^{\text{AL}c}(q) &= TU_d^4 \sum_p \Lambda_\alpha(q; p) \left[\frac{3}{2} \chi^{\text{spin}}(p+q) \chi^{\text{spin}}(p) \right. \\ &\quad \left. + \frac{1}{2} \chi^{\text{charge}}(p+q) \chi^{\text{charge}}(p) \right] \Lambda'_\beta(q; p), \end{aligned} \quad (\text{C2})$$

where $p = (\mathbf{p}, i\omega_n)$ and $\omega_n = 2\pi nT$. Here Λ_l and Λ'_l are the three-point vertices:

$$\begin{aligned} \Lambda_\alpha(q; p) &= T \sum_k f_\alpha\left(\mathbf{k} + \frac{\mathbf{q}}{2}\right) \\ &\quad \times G_{\alpha,d}(k+q) G_{d,d}(k-p) G_{d,\alpha}(k), \end{aligned} \quad (\text{C3})$$

$$\begin{aligned} \Lambda'_\beta(q; p) &= T \sum_{k'} f_\beta\left(k' + \frac{\mathbf{q}}{2}\right) G_{\beta,d}(k') [G_{d,d}(k'-p) \\ &\quad + G_{d,d}(k'+p+q)] G_{d,\beta}(k'+q). \end{aligned} \quad (\text{C4})$$

Their diagrammatic expressions are shown in Fig. 13.

For the d -orbital BDW with d -symmetry form factor, the form factors $f_\alpha(\mathbf{k})$ ($\alpha = d, x, y$) are set to

$$f_d(\mathbf{k}) = \cos(k_x) - \cos(k_y), \quad f_x(\mathbf{k}) = f_y(\mathbf{k}) = 0. \quad (\text{C5})$$

The form factors for the p -ODW with d symmetry are

$$f_d(\mathbf{k}) = 0, \quad f_x(\mathbf{k}) = +1, \quad f_y(\mathbf{k}) = -1, \quad (\text{C6})$$

and those with s' symmetry are

$$f_d(\mathbf{k}) = 0, \quad f_x(\mathbf{k}) = +1, \quad f_y(\mathbf{k}) = +1. \quad (\text{C7})$$

-
- [1] A. Bianconi, N. L. Saini, A. Lanzara, M. Missori, T. Rossetti, H. Oyanagi, H. Yamaguchi, K. Oka, and T. Ito, *Determination of the Local Lattice Distortions in the CuO₂ Plane of La_{1.85}Sr_{0.15}CuO₄*, Phys. Rev. Lett. **76**, 3412–3415 (1996).
- [2] T. Hanaguri, C. Lupien, Y. Kohsaka, D.-H. Lee, M. Azuma, M. Takano, H. Takagi, and J. C. Davis, *A ‘checkerboard’ electronic crystal state in lightly hole-doped Ca_{2-x}Na_xCuO₂Cl₂*, Nature **430**, 1001–1005 (2004).
- [3] R. Daou, J. Chang, D. LeBoeuf, O. Cyr-Choinière, F. Laliberté, N. Doiron-Leyraud, B. J. Ramshaw, R. Liang, D. A. Bonn, W. N. Hardy, and L. Taillefer, *Broken rotational symmetry in the pseudogap phase of a high-T_c superconductor*, Nature **463**, 519–522 (2010).
- [4] M. J. Lawler, K. Fujita, J. Lee, A. R. Schmidt, Y. Kohsaka, C. K. Kim, H. Eisaki, S. Uchida, J. C. Davis, J. P. Sethna, and E.-A. Kim, *Intra-unit-cell electronic nematicity of the high-T_c copper-oxide pseudogap states*, Nature **466**, 347–351 (2010).
- [5] M. Hücker, M. von Zimmermann, M. Debessai, J. S. Schilling, J. M. Tranquada, and G. D. Gu, *Spontaneous Symmetry Breaking by Charge Stripes in the High Pressure Phase of Superconducting La_{1.875}Ba_{0.125}CuO₄*, Phys. Rev. Lett. **104**, 057004 (2010).
- [6] M. Hücker, M. von Zimmermann, G. D. Gu, Z. J. Xu, J. S. Wen, G. Xu, H. J. Kang, A. Zheludev, and J. M. Tranquada, *Stripe or*

- der in superconducting $La_{2-x}Ba_xCuO_4$ ($0.095 \leq x \leq 0.155$), Phys. Rev. B **83**, 104506 (2011).
- [7] Y. Kohsaka, T. Hanaguri, M. Azuma, M. Takano, J. C. Davis, and H. Takagi, *Visualization of the emergence of the pseudogap state and the evolution to superconductivity in a lightly hole-doped Mott insulator*, Nat. Phys. **8**, 534–538 (2012).
- [8] G. Ghiringhelli, M. Le Tacon, M. Minola, S. Blanco-Canosa, C. Mazzoli, N. B. Brookes, G. M. De Luca, A. Frano, D. G. Hawthorn, F. He, T. Loew, M. M. Sala, D. C. Peets, M. Saluzzo, E. Schierle, R. Sutarto, G. A. Sawatzky, E. Weschke, B. Keimer, and L. Braicovich, *Long-Range Incommensurate Charge Fluctuations in $(Y,Nd)Ba_2Cu_3O_{6+x}$* , Science **337**, 821–825 (2012).
- [9] J. Chang, E. Blackburn, A. T. Holmes, N. B. Christensen, J. Larsen, J. Mesot, R. Liang, D. A. Bonn, W. N. Hardy, A. Watenphul, M. von Zimmermann, E. M. Forgan, and S. M. Hayden, *Direct observation of competition between superconductivity and charge density wave order in $YBa_2Cu_3O_{6.67}$* , Nat. Phys. **8**, 871–876 (2012).
- [10] T. Wu, H. Mayaffre, S. Krämer, M. Horvatić, C. Berthier, P. L. Kuhns, A. P. Reyes, R. Liang, W. N. Hardy, D. A. Bonn, and M.-H. Julien, *Emergence of charge order from the vortex state of a high-temperature superconductor*, Nat. Comms. **4**, 2113 (2013).
- [11] E. Blackburn, J. Chang, M. Hücker, A. T. Holmes, N. B. Christensen, R. Liang, D. A. Bonn, W. N. Hardy, U. Rütt, O. Gutowski, M. v. Zimmermann, E. M. Forgan, and S. M. Hayden, *X-Ray Diffraction Observations of a Charge-Density-Wave Order in Superconducting Ortho-II $YBa_2Cu_3O_{6.54}$ Single Crystals in Zero Magnetic Field*, Phys. Rev. Lett. **110**, 137004 (2013).
- [12] K. Fujita, M. H. Hamidian, S. D. Edkins, C. K. Kim, Y. Kohsaka, M. Azuma, M. Takano, H. Takagi, H. Eisaki, S. Uchida, A. Allais, M. J. Lawler, E. A. Kim, S. Sachdev, and J. C. Davis, *Direct phase-sensitive identification of a d-form factor density wave in underdoped cuprates*, Proc. Natl. Acad. Sci. USA **111**, E3026–E3032 (2014).
- [13] R. Comin, A. Frano, M. M. Yee, Y. Yoshida, H. Eisaki, E. Schierle, E. Weschke, R. Sutarto, F. He, A. Soumyanarayanan, Y. He, M. Le Tacon, I. S. Elfimov, J. E. Hoffman, G. A. Sawatzky, B. Keimer, and A. Damascelli, *Charge Order Driven by Fermi-Arc Instability in $Bi_2Sr_{2-x}La_xCuO_{6+\delta}$* , Science **343**, 390–392 (2014).
- [14] E. da Silva Neto, P. Aynajian, A. Frano, R. Comin, E. Schierle, E. Weschke, A. Gyenis, J. Wen, J. Schneeloch, Z. Xu, S. Ono, G. Gu, M. Le Tacon, and A. Yazdani, *Ubiquitous Interplay Between Charge Ordering and High-Temperature Superconductivity in Cuprates*, Science **343**, 393–396 (2014).
- [15] W. Tabis, Y. Li, M. Le Tacon, L. Braicovich, A. Kreyssig, M. Minola, G. Dellea, E. Weschke, M. J. Veit, M. Ramanoglu, A. I. Goldman, T. Schmitt, G. Ghiringhelli, N. Barisić, M. K. Chan, C. J. Dorow, G. Yu, X. Zhao, B. Keimer, and M. Greven, *Charge order and its connection with Fermi-liquid charge transport in a pristine high-T_c cuprate*, Nat. Comms. **5**, 5875 (2014).
- [16] T. Wu, H. Mayaffre, S. Krämer, M. Horvatić, C. Berthier, W. N. Hardy, R. Liang, D. A. Bonn, and M.-H. Julien, *Inipient charge order observed by NMR in the normal state of $YBa_2Cu_3O_y$* , Nat. Comms. **6**, 6438 (2015).
- [17] M. H. Hamidian, S. D. Edkins, C. K. Kim, J. C. Davis, A. P. Mackenzie, H. Eisaki, S. Uchida, M. J. Lawler, E. A. Kim, S. Sachdev, and K. Fujita, *Atomic-scale electronic structure of the cuprate d-symmetry form factor density wave state*, Nat. Phys. (2015).
- [18] E. H. da Silva Neto, R. Comin, F. He, R. Sutarto, Y. Jiang, R. L. Greene, G. A. Sawatzky, and A. Damascelli, *Charge ordering in the electron-doped superconductor $Nd_{2-x}Ce_xCuO_4$* , Science **347**, 282–285 (2015).
- [19] R. Comin, R. Sutarto, E. H. da Silva Neto, L. Chauviere, R. Liang, W. N. Hardy, D. A. Bonn, F. He, G. A. Sawatzky, and A. Damascelli, *Broken translational and rotational symmetry via charge stripe order in underdoped $YBa_2Cu_3O_{6+y}$* , Science **347**, 1335–1339 (2015).
- [20] R. Comin, R. Sutarto, F. He, E. H. da Silva Neto, L. Chauviere, A. Frano, R. Liang, W. N. Hardy, D. A. Bonn, Y. Yoshida, H. Eisaki, A. J. Achkar, D. G. Hawthorn, B. Keimer, G. A. Sawatzky, and A. Damascelli, *Symmetry of charge order in cuprates*, Nat. Mater. **14**, 796–800 (2015).
- [21] R. Comin and A. Damascelli, *Resonant x-ray scattering studies of charge order in cuprates*, Annu. Rev. Condens. Matter Phys. **7**, 369 (2016).
- [22] P. W. Anderson, *The Resonating Valence Bond State in La_2CuO_4 and Superconductivity*, Science **235**, 1196–1198 (1987).
- [23] C. M. Varma, *Pseudogap Phase and the Quantum-Critical Point in Copper-Oxide Metals*, Phys. Rev. Lett. **83**, 3538–3541 (1999).
- [24] V. J. Emery and S. A. Kivelson, *Importance of phase fluctuations in superconductors with small superfluid density*, Nature **374**, 434–437 (1995).
- [25] P. A. Lee, N. Nagaosa, and X.-G. Wen, *Doping a Mott insulator: Physics of high-temperature superconductivity*, Rev. Mod. Phys. **78**, 17–85 (2006).
- [26] A.-M. S. Tremblay, *Two-Particle-Self-Consistent Approach for the Hubbard Model, Strongly Correlated Systems*, A. Avella and F. P. Mancini, eds. (Springer Berlin Heidelberg, Berlin, Heidelberg, 2012), pp. 409–453.
- [27] J. C. Davis and D.-H. Lee, *Concepts relating magnetic interactions, intertwined electronic orders, and strongly correlated superconductivity*, Proc. Natl. Acad. Sci. USA **110**, 17623–17630 (2013).
- [28] M. A. Metlitski and S. Sachdev, *Quantum phase transitions of metals in two spatial dimensions. II. Spin density wave order*, Phys. Rev. B **82**, 075128 (2010).
- [29] M. A. Metlitski and S. Sachdev, *Instabilities near the onset of spin density wave order in metals*, New J. Phys. **12**, 105007 (2010).
- [30] T. Holder and W. Metzner, *Incommensurate nematic fluctuations in two-dimensional metals*, Phys. Rev. B **85**, 165130 (2012).
- [31] C. Husemann and W. Metzner, *Incommensurate nematic fluctuations in the two-dimensional Hubbard model*, Phys. Rev. B **86**, 085113 (2012).
- [32] K. B. Efetov, H. Meier, and C. Pépin, *Pseudogap state near a quantum critical point*, Nat. Phys. **9**, 442–446 (2013).
- [33] S. Sachdev and R. La Placa, *Bond Order in Two-Dimensional Metals with Antiferromagnetic Exchange Interactions*, Phys. Rev. Lett. **111**, 027202 (2013).
- [34] C. Pépin, V. S. de Carvalho, T. Kloss, and X. Montiel, *Pseudogap, charge order, and pairing density wave at the hot spots in cuprate superconductors*, Phys. Rev. B **90**, 195207 EP– (2014).
- [35] A. Allais, J. Bauer, and S. Sachdev, *Density wave instabilities in a correlated two-dimensional metal*, Phys. Rev. B **90**, 155114 (2014).
- [36] D. Chowdhury and S. Sachdev, *Feedback of superconducting fluctuations on charge order in the underdoped cuprates*, Phys. Rev. B **90**, 134516 (2014).
- [37] S. Whitsitt and S. Sachdev, *Renormalization group analysis of*

- a fermionic hot-spot model*, Phys. Rev. B **90**, 104505 (2014).
- [38] E. Berg, E. Fradkin, S. A. Kivelson, and J. M. Tranquada, *Striped superconductors: how spin, charge and superconducting orders intertwine in the cuprates*, New J. Phys. **11**, 115004 (2009).
- [39] P. A. Lee, *Amperean Pairing and the Pseudogap Phase of Cuprate Superconductors*, Phys. Rev. X **4**, 031017 (2014).
- [40] E. Fradkin, S. A. Kivelson, and J. M. Tranquada, *Colloquium: Theory of intertwined orders in high temperature superconductors*, Rev. Mod. Phys. **87**, 457–482 (2015).
- [41] Y. Wang, D. F. Agterberg, and A. V. Chubukov, *Interplay between pair- and charge-density-wave orders in underdoped cuprates*, Phys. Rev. B **91**, 115103 (2015).
- [42] Y. Wang, D. F. Agterberg, and A. V. Chubukov, *Coexistence of Charge-Density-Wave and Pair-Density-Wave Orders in Underdoped Cuprates*, Phys. Rev. Lett. **114**, 197001 (2015).
- [43] Y. Wang and A. V. Chubukov, *Charge-density-wave order with momentum (2Q,0) and (0,2Q) within the spin-fermion model: Continuous and discrete symmetry breaking, preemptive composite order, and relation to pseudogap in hole-doped cuprates*, Phys. Rev. B **90**, 035149 (2014).
- [44] A. M. Tsvelik and A. V. Chubukov, *Composite charge order in the pseudogap region of the cuprates*, Phys. Rev. B **89**, 184515 (2014).
- [45] V. Mishra and M. R. Norman, *Strong coupling critique of spin fluctuation driven charge order in underdoped cuprates*, Phys. Rev. B **92**, 060507 (2015).
- [46] Y. Yamakawa and H. Kontani, *Spin-Fluctuation-Driven Nematic Charge-Density Wave in Cuprate Superconductors: Impact of Aslamazov-Larkin Vertex Corrections*, Phys. Rev. Lett. **114**, 257001 (2015).
- [47] J. Sólyom, *The Fermi gap model of one-dimensional conductors*, Adv. Phys. **28**, 201–303 (1979).
- [48] C. Bourbonnais, B. Guay, and R. Wortis, *Renormalization Group Technique for Quasi-One-Dimensional Interacting Fermion Systems at Finite Temperature, Theoretical Methods for Strongly Correlated Electrons*, D. Sénéchal, A.-M. Tremblay, and C. Bourbonnais, eds. (Springer, New York, 2004), pp. 77–137.
- [49] D. Zanchi and H. J. Schulz, *Weakly correlated electrons on a square lattice: A renormalization group theory*, Europhys. Lett. **44**, 235–241 (1998).
- [50] C. J. Halboth and W. Metzner, *d-wave superconductivity and Pomeranchuk instability in the two-dimensional Hubbard model*, Phys. Rev. Lett. **85**, 5162–5165 (2000).
- [51] C. J. Halboth and W. Metzner, *Renormalization-group analysis of the two-dimensional Hubbard model*, Phys. Rev. B **61**, 7364–7377 (2000).
- [52] C. Honerkamp, M. Salmhofer, N. Furukawa, and T. M. Rice, *Breakdown of the Landau-Fermi liquid in two dimensions due to umklapp scattering*, Phys. Rev. B **63**, 035109 (2001).
- [53] C. Honerkamp and M. Salmhofer, *Temperature-flow renormalization group and the competition between superconductivity and ferromagnetism*, Phys. Rev. B **64**, 184516 (2001).
- [54] C. Honerkamp, *Charge instabilities at the metamagnetic transition of itinerant electron systems*, Phys. Rev. B **72**, 115103 (2005).
- [55] F. Wang, H. Zhai, Y. Ran, A. Vishwanath, and D.-H. Lee, *Functional Renormalization-Group Study of the Pairing Symmetry and Pairing Mechanism of the FeAs-Based High-Temperature Superconductor*, Phys. Rev. Lett. **102**, 047005 (2009).
- [56] W. Metzner, M. Salmhofer, C. Honerkamp, V. Meden, and K. Schönhammer, *Functional renormalization group approach to correlated fermion systems*, Rev. Mod. Phys. **84**, 299–352 (2012).
- [57] Q. H. Wang, C. Platt, Y. Yang, C. Honerkamp, F.-C. Zhang, W. Hanke, T. M. Rice, and R. Thomale, *Theory of superconductivity in a three-orbital model of Sr_2RuO_4* , Europhys. Lett. **104**, 17013 (2013).
- [58] M. Tsuchizawa, Y. Ohno, S. Onari, and H. Kontani, *Orbital Nematic Instability in the Two-Orbital Hubbard Model: Renormalization-Group + Constrained RPA Analysis*, Phys. Rev. Lett. **111**, 057003 (2013).
- [59] M. Tsuchizawa, Y. Yamakawa, S. Onari, Y. Ohno, and H. Kontani, *Spin-triplet superconductivity in Sr_2RuO_4 due to orbital and spin fluctuations: Analyses by two-dimensional renormalization group theory and self-consistent vertex-correction method*, Phys. Rev. B **91**, 155103 (2015).
- [60] V. J. Emery, *Theory of high- T_c superconductivity in oxides*, Phys. Rev. Lett. **58**, 2794–2797 (1987).
- [61] C. M. Varma, S. Schmitt-Rink, and E. Abrahams, *Charge transfer excitations and superconductivity in “ionic” metals*, Solid State Commun. **62**, 681–685 (1987).
- [62] S. Bulut, W. A. Atkinson, and A. P. Kampf, *Spatially modulated electronic nematicity in the three-band model of cuprate superconductors*, Phys. Rev. B **88**, 155132 (2013).
- [63] A. Thomson and S. Sachdev, *Charge ordering in three-band models of the cuprates*, Phys. Rev. B **91**, 115142 (2015).
- [64] P. Hansmann, N. Parragh, A. Toschi, G. Sangiovanni, and K. Held, *Importance of d-p Coulomb interaction for high T_c cuprates and other oxides*, New J. Phys. **16**, 033009 (2014).
- [65] In this paper, we used the “0MTO hopping integrals” in Ref. [64]. We verified that numerical results are unchanged if another set of “IMTO hopping integrals” in Ref. [64] is used.
- [66] H. Kontani, *Anomalous transport phenomena in Fermi liquids with strong magnetic fluctuations*, Rep. Prog. Phys. **71**, 026501 (2008).
- [67] S. Gerber, H. Jang, H. Nojiri, S. Matsuzawa, H. Yasumura, D. A. Bonn, R. Liang, W. N. Hardy, Z. Islam, A. Mehta, S. Song, M. Sikorski, D. Stefanescu, Y. Feng, S. A. Kivelson, T. P. Devereaux, Z. X. Shen, C. C. Kao, W. S. Lee, D. Zhu, and J. S. Lee, *Three-dimensional charge density wave order in $YBa_2Cu_3O_{6.67}$ at high magnetic fields*, Science **350**, 949–952 (2015).
- [68] J. Chang, E. Blackburn, O. Ivashko, A. T. Holmes, N. B. Christensen, M. Hücker, R. Liang, D. A. Bonn, W. N. Hardy, U. Rütt, M. von Zimmermann, E. M. Forgan, and S. M. Hayden, *Magnetic field controlled charge density wave coupling in underdoped $YBa_2Cu_3O_{6+x}$* , arXiv:1511.06092 (2015).
- [69] C. Stock, W. J. L. Buyers, R. Liang, D. Peets, Z. Tun, D. A. Bonn, W. N. Hardy, and R. J. Birgeneau, *Dynamic stripes and resonance in the superconducting and normal phases of $YBa_2Cu_3O_{6.5}$ ortho-II superconductor*, Phys. Rev. B **69**, 014502 (2004).
- [70] S. Caprara, C. Di Castro, M. Grilli, and D. Suppa, *Charge-Fluctuation Contribution to the Raman Response in Superconducting Cuprates*, Phys. Rev. Lett. **95**, 117004 (2005).
- [71] L. Tassini, F. Venturini, Q. M. Zhang, R. Hackl, N. Kikugawa, and T. Fujita, *Dynamical Properties of Charged Stripes in $La_{2-x}Sr_xCuO_4$* , Phys. Rev. Lett. **95**, 117002 (2005).
- [72] T. P. Devereaux and R. Hackl, *Inelastic light scattering from correlated electrons*, Rev. Mod. Phys. **79**, 175–233 (2007).
- [73] E. M. Forgan, E. Blackburn, A. T. Holmes, A. Briffa, J. Chang, L. Bouchenoire, S. D. Brown, R. Liang, D. A. Bonn, W. N. Hardy, N. B. Christensen, M. von Zimmermann, M. Huecker, and S. M. Hayden, *The nature of the charge density waves in under-doped $YBa_2Cu_3O_{6.54}$ revealed by X-ray measurements of the ionic displacements*, arXiv:1504.01585 (2015).

- [74] S. Kasahara, H. J. Shi, K. Hashimoto, S. Tonegawa, Y. Mizukami, T. Shibauchi, K. Sugimoto, T. Fukuda, T. Terashima, A. H. Nevidomskyy, and Y. Matsuda, *Electronic nematicity above the structural and superconducting transition in $BaFe_2(As_{1-x}P_x)_2$* , *Nature* **486**, 382–385 (2012).
- [75] R. M. Fernandes, L. VanBebber, S. Bhattacharya, P. Chandra, V. Keppens, D. Mandrus, M. McGuire, B. Sales, A. Sefat, and J. Schmalian, *Effects of Nematic Fluctuations on the Elastic Properties of Iron Arsenide Superconductors*, *Phys. Rev. Lett.* **105**, 157003 (2010).
- [76] S. Onari and H. Kontani, *Self-consistent Vertex Correction Analysis for Iron-based Superconductors: Mechanism of Coulomb Interaction-Driven Orbital Fluctuations*, *Phys. Rev. Lett.* **109**, 137001 (2012).
- [77] H. Kontani and Y. Yamakawa, *Linear Response Theory for Shear Modulus C_{66} and Raman Quadrupole Susceptibility: Evidence for Nematic Orbital Fluctuations in Fe-based Superconductors*, *Phys. Rev. Lett.* **113**, 047001 (2014).
- [78] S. A. Maier, J. Ortloff, and C. Honerkamp, *Multiorbital effects in the functional renormalization group: A weak-coupling study of the Emery model*, *Phys. Rev. B* **88**, 235112 (2013).